coatings

MDPI

Article

Mechanochemical Nano-Welding and Self-Locking Kinetics of CNTs During PEEK Surface Nanomodification via Cold Spraying

Oleksandr Hondliakh [1,2,*], Illia Yankovskyi [1] and Sergiy Antonyuk [2]

[1] Igor Sikorsky Kyiv Polytechnic Institute, National Technical University of Ukraine, 37, Beresteiskyi Ave, 03056 Kyiv, Ukraine; il.yankovskyi@gmail.com

[2] RPTU University Kaiserslautern-Landau, 47, 67663 Kaiserslautern, Germany; sergiy.antonyuk@mv.rptu.de

* Correspondence: oleksandr.hondliakh@rptu.de; Tel.: +49-151-5653-1226

Abstract

This study addresses a critical challenge in surface engineering: developing robust nanocomposite layers on high-performance thermoplastics without inducing macroscopic thermal degradation. While cold gas dynamic spraying (CGDS) of polymers is often described in the literature as a deposition process based on purely mechanical anchoring of particles into polymer surface, our work establishes a multi-scale, hybrid physical–chemical adhesion framework. Using a coupled 3D thermoplasticity finite element model with a Mie–Grüneisen equation of state and Johnson–Cook criteria, we evaluate the supersonic impact dynamics ($V_0 = 1000$ m/s) of single-walled (5,0) CNTs impacting a PEEK substrate at oblique angles (0–20°). The core scientific lies in bridging continuum mechanics with quantum-chemical statistics. By applying Weibull weakest-link theory to a 37-bond monomer model, we demonstrate that compliant $C_{arom} - O$ ether bonds selectively absorb impact energy, covering 8.37% of their dissociation barrier. This non-uniform energy sharing yields a 0.23% monomer activation probability, generating a high free-radical density of ~1100 μm^{-2} beneath the particle plume. This localized "chemical nano-welding" network provides exceptional chemical adhesion, while the remaining 99.77% of intact chains ensure structural rigidity, reinforced by a mechanical "self-locking" field (residual compressive stresses up to 0.9 GPa). This study provides a scientific foundation for designing functional coatings tailored for engineering, aerospace, and biomedical applications.

Keywords: cold gas spraying; PEEK; CNT; supersonic impact; FEM; surface nanomodification; mechanical interlocking

Check for updates

Academic Editors: Neringa Petrašauskienė and Ingrida Ancutiene

Received: 26 May 2026

Revised: 1 July 2026

Accepted: 8 July 2026

Published: 15 July 2026

1. Introduction

The cold gas dynamic spraying (CGDS) process has firmly established itself as a highly efficient, solid-state deposition technology for applying functional coatings onto metallic and polymeric substrates, providing reliable protection against corrosion, erosion, and wear [1–8]. This method finds widespread application across mechanical engineering, aerospace, automotive, energy, medical, and chemical industries [3–5]. Additionally, CGDS is successfully utilized for surface modification and microstructuring of substrates to improve their tribological characteristics and impart engineered functional properties to the target surfaces [6–8].

The principal distinction of CGDS from conventional thermal spraying methodologies lies in the fact that its operational process occurs at temperatures substantially below the melting point of the sprayed material. Particle consolidation onto the substrate is achieved

 https://doi.org/10.3390/coatings16070843

exclusively through the kinetic energy of a supersonic gas stream, which initiates intensive plastic deformation within the contact zone upon impact [9,10]. This mechanism minimizes the thermal impact on the substrate microstructure and prevents oxidation of the sprayed particles, thereby ensuring high cohesive strength and density of the resulting coatings [11].

Specifically, CGDS can facilitate internal cohesive strengths via ductile metallurgical bonding at the splat-to-splat interfaces in the range of 30–50 MPa. Concurrently, the resulting interfacial adhesive strength on thermoplastic substrates varies from 0.2 to 14 MPa for conventional Cu/Cu/polyether ether ketone (PEEK) pairs, scaling up to 24 MPa for high-strength aluminum alloys (e.g., Al 7075) deposited on pure PEEK under optimized high-pressure conditions [5].

Particular practical significance is attributed to the application of CGDS for the metallization and nanomodification of polymeric substrates. Owing to the low thermal stability of engineering polymers, classical high-temperature spraying techniques carry an inherent risk of thermal degradation within the near-surface layer. Compared with alternative technologies—including physical vapor deposition (PVD), chemical vapor deposition (CVD), and electrochemical deposition (ECD)—the CGDS method delivers a substantially reduced thermal load on the substrate while maintaining high productivity and environmental safety [12].

Crucially, minimizing this thermal loading eliminates the risk of macro-scale thermal distortion (warping) and prevents the localized degradation of the polymer's macromolecular chains. Furthermore, preserving low process temperatures maintains the baseline matrix crystallinity of semi-crystalline polymers like PEEK and suppresses interfacial micro-cracking induced by thermal stress from the mismatch of coefficients of thermal expansion (CTE) between the deposit and the substrate. Consequently, this approach has already achieved widespread recognition in the aerospace sector, automotive manufacturing, electronics, and energy applications [13].

A promising yet insufficiently explored avenue involves the use of CGDS for incorporating carbon nanotubes (CNTs) into the surface layer of high-performance thermoplastic polymers—specifically, polyether ether ketone (PEEK). PEEK is widely utilized in demanding sectors such as aerospace, medical equipment, electronics, and mechanical engineering, owing to its combination of high thermal stability, exceptional mechanical strength, chemical inertness, and biocompatibility. However, it does possess certain drawbacks, such as limited surface wear resistance. Consequently, to enhance the wear resistance and durability of PEEK components, surface hardening and functionalization using CNTs are essential.

The published literature describes examples of the successful metallization of PEEK substrates via CGDS [14], whereas bulk modification of PEEK with carbon nanostructures using conventional mixing techniques has demonstrated substantial improvements in the electrophysical and tribological properties of the material [15,16]. However, bulk filler incorporation inevitably alters the macroscopic characteristics of the entire component. Employing CGDS for localized CNT embedding directly into the PEEK surface layer represents a fundamentally different strategy, confining functionalization exclusively to the near-surface zone without affecting the bulk characteristics of the base material. Nevertheless, systematic numerical and experimental investigations into the kinetics of such interactions are completely absent from the literature. Concurrently, the physical nature governing the bonding of nanostructures with an extremely high aspect ratio under supersonic impact must fundamentally differ from the mechanics of micrometer-scale metallic particles; beyond simple mechanical anchoring, it may encompass mechanisms of localized mechanochemical activation of the polymer chains.

The fundamental principle of the CGDS method is based on the acceleration of powder particles by a supersonic gas flow in a de Laval nozzle, where the total enthalpy of the gas (including the thermodynamic component and the kinetic energy of the high-velocity flow) is converted into the kinetic energy of the sprayed material, with the transfer of mechanical momentum from the gas to the particles prevailing over the thermal effect [17–19]. Coating formation occurs exclusively when the particle reaches a critical impact velocity V_{cr}—a threshold value below which adhesion to the substrate is not initiated [7,13,17,20]. For metallic particles in the micron size range (1–50 μm), the impact velocity typically ranges from 300 to 1200 m/s, depending on the material properties, gas temperature, and gas pressure [5,6,14,15,17,21].

During deposition onto polymeric substrates, high-performance thermoplastics such as PEEK, polyetherimide (PEI), and acrylonitrile-butadiene-styrene (ABS) are recognized as the most promising matrix materials [22–24]. Unlike metallic substrates, polymers exhibit low resistance to erosive wear. For this class of materials, a strict viable "processing window" exists within the coordinates of the CGDS parameters, inside of which the kinetic energy of the particles is sufficient for their mechanical and chemical embedding without exceeding the threshold at which surface erosion begins to dominate the substrate [25–27].

PEEK is a semi-crystalline thermoplastic material with a glass transition temperature $T_g \approx 416$ K and a melting temperature $T_m \approx 524$ K [28]. These properties ensure the preservation of the matrix structural integrity under the dynamic thermal loads arising during the CGDS process. Within the temperature range from T_g to T_m, PEEK transitions into a highly elastic state, which drastically reduces the penetration resistance, facilitates encapsulation of the embedded nanostructures by the deformed polymer framework, and ensures their robust fixation upon system cooling.

The dominant adhesion mechanism during coating deposition onto PEEK is widely considered to be mechanical anchoring: a portion of the impact kinetic energy dissipates as heat, inducing instantaneous localized softening of the near-surface polymer layer, which enables particle embedding and subsequent geometric interlocking [28–32]. This retention mechanism has been experimentally validated for micron-sized metallic coatings on PEEK substrates [32].

However, for carbon nanotubes—which possess an extraordinary axial Young's modulus of approximately 1 TPa, a longitudinal tensile strength of 50–100 GPa, an ultra-small outer diameter of 0.8–2.0 nm, and a high aspect ratio (>1000) [31]—the bonding mechanics must exhibit a more complex, hybrid physical–chemical nature.

Extreme localized pressures within the contact zone between the nanostructure and the matrix are capable of triggering the selective mechanochemical cleavage of the most vulnerable polymer linkages. The free radicals generated in this process can provide direct chemisorption onto the structural defects of the CNT lattice, translating adhesion to a qualitatively new quantum-chemical level ("nano-welding"), the theoretical models of which for oblique impact CGDS systems have not yet been reported in the literature.

The spray angle is a key technological parameter determining the microstructure and adhesion characteristics of the deposited coating. For classical metallic systems (such as Ti, Ni, Cu, and Inconel 718), deviations of the particle velocity vector from the surface normal systematically degrade adhesion due to the redistribution of kinetic energy toward the tangential component [32–35]. The gas jet exiting the Laval nozzle exhibits an intrinsic divergence half-angle in the range of 1–5° [36,37]. However, the actual impact angle of individual particles can vary considerably beyond this value. Upon jet impingement onto the substrate surface, a stagnation zone forms surrounded by a region of turbulent vortices [38]. Due to this flow deflection effect, fine particles with low inertia are carried

https://doi.org/10.3390/coatings16070843

by the turbulent eddies and deviate significantly from the nozzle axis, establishing a wide distribution of impact angles within the spray spot boundary [39,40].

Under normal impact (90°), symmetric material jetting forms in the contact zone, maximizing the active contact area. Under oblique impact, this process becomes asymmetric, leading to an increase in porosity and a reduction in deposition efficiency; furthermore, at impact angles of approximately 45° or less for micron-sized metallic particles, elastic rebound begins to predominate, precluding stable adhesion [41,42]. Nevertheless, the mechanics governing the high-velocity interaction of rigid, extended nanostructures with elastic-plastic polymer matrices under the conditions of oblique CGDS impact remain completely unexamined.

The objective of the present study is to establish the governing patterns of the impact angle influence on the embedding dynamics, spatial stabilization, and kinetics of hybrid mechanochemical adhesion formation of a single carbon nanotube within a thermoplastic PEEK matrix. This is achieved through the finite element modeling, evaluated at an impact velocity corresponding to the baseline processing regime.

To achieve this stated objective, the following tasks are addressed: development of a spatial finite element model for the coupled thermoplasticity problem governing the high-velocity impact of a single CNT onto a PEEK substrate, incorporating the adiabatic softening and failure criteria of the matrix; numerical investigation into the effect of the impact angle (0°, 5°, 10°, 20°) on the stress fields, plastic strain distributions, thermal gradients, and relaxation kinetics within the contact zone; development of a multi-scale theoretical model to evaluate the probability of selective chemical bond cleavage within PEEK and the subsequent quantum-chemical fixation of the CNT based on the thermomechanical energy balance and the statistical weakest-link theory.

2. Materials and Methods

The equations of the coupled thermoplasticity problem describe the simultaneous effect of thermal fields on the mechanical state of the material (stresses and strains) and, conversely, the influence of plastic deformation on the temperature distribution via energy dissipation. The complete set of governing equations comprises:

1. **Equations of Motion:**

$$\nabla \cdot \boldsymbol{\sigma} + \mathbf{f} = \rho \ddot{\mathbf{u}}\text{ in terms of displacements} \tag{1}$$

or

$$\nabla \cdot \boldsymbol{\sigma} + \mathbf{f} = \rho \dot{\mathbf{v}}\text{ in terms of velocities,} \tag{2}$$

where $\boldsymbol{\sigma}$ is the stress tensor; $\mathbf{f}$ is the body force vector; $\mathbf{u}$ is the displacement vector; $\mathbf{v}$ is the velocity vector; $\boldsymbol{\nabla}$ denotes the gradient operator; and $\boldsymbol{\nabla}$ represents the divergence operator.

2. **Kinematic Equations:**

$$\varepsilon = \frac{1}{2}\left(\nabla \mathbf{u} + (\nabla \mathbf{u})^{T}\right) = \varepsilon^{e} + \varepsilon^{p} + \varepsilon^{T}, \tag{3}$$

where ε is the total strain tensor; ε^{e} is the elastic strain tensor; ε^{p} is the plastic strain tensor; $\varepsilon^{T} = \boldsymbol{\alpha}_T(T - T_0)$ is the thermal strain tensor; $\boldsymbol{\alpha}_T$ is the second-order thermal expansion tensor; and T_0 is the reference (initial) temperature of the body.

For an isotropic material (such as PEEK), the thermal strain tensor simplifies to:

$$\varepsilon^{T} = \alpha_T (T - T_0)\mathbf{I},$$

where α_T is the scalar coefficient of linear thermal expansion for an isotropic body, and $\mathbf{I}$ is the second-order identity tensor.

3. **Constitutive (Physical) Equations:**

$$\boldsymbol{\sigma} = \mathbf{C}:[(\varepsilon^{e} - \boldsymbol{\alpha}_{T}(T - T_{0})]^{-}\text{Duhamel–Neumann law},$$

where **C** is the fourth-order stiffness tensor containing the physical–mechanical deformation constants of the material.

4. **Plastic Flow Rule (Constitutive Equations of Plasticity):**

$$\mathbf{d}\varepsilon^{\mathbf{p}} = \mathbf{d}\boldsymbol{\gamma}\frac{\partial F}{\partial \boldsymbol{\sigma}}, \tag{4}$$

where $\mathbf{d}\varepsilon^{\mathbf{p}}$ is the plastic strain increment tensor; $\boldsymbol{\gamma}$ is a positive scalar multiplier of proportionality (the plastic multiplier) with $\mathbf{d}\boldsymbol{\gamma} > 0$; F is the yield function (yield surface) defining the boundary of the elastic domain in stress space (e.g., the von Mises yield criterion); $\frac{\partial F}{\partial \boldsymbol{\sigma}}$ is the gradient of the yield function, representing the outward normal vector to the yield surface at the point corresponding to the current stress state.

The total strain velocity tensor **D** is defined as:

$$\mathbf{D} = \dot{\varepsilon} = \frac{1}{2}\left(\nabla\mathbf{v} + (\nabla\mathbf{v})^{T}\right) = \mathbf{D}^{e} + \mathbf{D}^{p}, \tag{5}$$

where **D** is the total strain rate tensor; $\mathbf{D}^{e}$ is the elastic strain rate tensor; $\mathbf{D}^{p} = \dot{\varepsilon}^{P} = \dot{\gamma}\frac{\partial F(\boldsymbol{\sigma})}{\partial \boldsymbol{\sigma}}$ is the plastic strain rate tensor; $\dot{\gamma}$ is the plastic multiplier (a scalar parameter governing plastic loading) with $\dot{\gamma} > 0$; $\frac{\partial F(\boldsymbol{\sigma})}{\partial \boldsymbol{\sigma}}$ is the gradient tensor of the yield function, oriented along the outward normal to the yield surface $F(\boldsymbol{\sigma}) = 0$.

In dynamic problems, the flow rule is typically supplemented by an evolution equation for the stress rate, commonly expressed in the rate form of the Duhamel–Neumann law, which accounts for the rigid-body rotation of the material, namely:

$$\dot{\boldsymbol{\sigma}}^{\omega} = \dot{\boldsymbol{\sigma}} + \boldsymbol{\sigma}\cdot\mathbf{W} - \mathbf{W}\cdot\boldsymbol{\sigma}, \tag{6}$$

where $\dot{\boldsymbol{\sigma}}^{\omega}$ is the Jaumann objective rate of the stress tensor $\boldsymbol{\sigma}$;

$$\dot{\boldsymbol{\sigma}} = \mathbf{C}:\left[\mathbf{D}^{e} - \boldsymbol{\alpha}_{T}\dot{T}\right] = \mathbf{C}:\left[\left((\mathbf{D} - \mathbf{D}^{\mathbf{p}}) - \boldsymbol{\alpha}_{\mathbf{T}}\dot{\mathbf{T}}\right)\right]; \tag{7}$$

$\mathbf{W} = \frac{1}{2}\left(\nabla\mathbf{v} - (\nabla\mathbf{v})^{T}\right)$ is the tensor, defined as the antisymmetric part of the velocity gradient; $\dot{T}$ is the material time derivative of temperature.

Under the assumption of small rotations, the Jaumann rate simplifies to the standard material derivative: $\dot{\boldsymbol{\sigma}}^{\omega} = \dot{\boldsymbol{\sigma}}$.

5. **Thermal Energy Balance (Heat Conduction Equation with Dissipation):**

$$\rho c_{v}\dot{T} = \nabla\cdot(\boldsymbol{\lambda}\cdot\nabla T) + \beta\left(\boldsymbol{\sigma}:\dot{\varepsilon}^{P}\right) + \mathbf{Q}, \tag{8}$$

where $\rho c_{v}\dot{T}$ represents the rate of change in internal energy (ρ is the density, and c_{v} is the specific heat capacity); $\boldsymbol{\lambda}$ is the thermal conductivity tensor; ∇T is the temperature gradient; $\boldsymbol{\sigma}:\dot{\varepsilon}^{P}$ is the volumetric heat source generated by plastic dissipation (plastic deformation work);

$\beta \leq 1$ is the Taylor–Quinney coefficient, which specifies the fraction of plastic work converted into thermal energy; **Q** represents external volumetric heat sources.

In this study, the phenomenological Johnson–Cook constitutive model [32,34,38] is utilized to simulate supersonic dynamic processes, explicitly accounting for the coupled effects of strain hardening, strain rate sensitivity, and adiabatic thermal softening. Accordingly, the equivalent yield stress of the PEEK material (σ_y) is computed using the classical multiplicative scalar relationship:

$$\sigma_y\left(\bar{\varepsilon}^p, \dot{\bar{\varepsilon}}^p, T\right) = [A + B(\bar{\varepsilon}^p)^n]\left[1 + C\ln\left(\frac{\dot{\bar{\varepsilon}}^p}{\dot{\varepsilon}_0}\right)\right]\left[1 - \left(\frac{T - T_r}{T_m - T_r}\right)^m\right], \quad (9)$$

where $\bar{\varepsilon}^p = \int_0^t \sqrt{\frac{2}{3}\dot{\boldsymbol{\varepsilon}}^p{:}\dot{\boldsymbol{\varepsilon}}^p}dt$ is the equivalent accumulated plastic strain; $\dot{\bar{\varepsilon}}^p$ is the equivalent plastic strain rate; $\dot{\varepsilon}_0$ is the reference strain rate (typically taken as 1.0 s^{-1}); T, T_r, T_m are the current temperature, reference (room) temperature, and melting temperature of the material, respectively; A is the initial yield stress; B is the strain hardening coefficient; n is the strain hardening exponent; C is the strain rate sensitivity coefficient; and m is the thermal softening exponent.

The application of the Johnson–Cook model for PEEK under supersonic impact conditions is well justified, as extremely high strain rates exceeding 10^6 s^{-1} and hydrodynamic pressures approaching 1 GPa drive this high-performance thermoplastic into a rheological regime that resembles the behavior of ductile metals [43]. Under these extreme conditions, the deformation kinetic is strictly dominated by viscoplastic flow, strong strain-rate sensitivity, and rapid adiabatic thermal softening, all of which are phenomenologically captured by the Johnson–Cook constitutive formulation with a high degree of mathematical efficiency. The Johnson–Cook constitutive parameters for PEEK were adopted from [20,28,29], where they were calibrated via dynamic compression data specifically tailored for high-velocity cold spray impact conditions on PEEK substrates and implemented within Abaqus/Explicit. The simulation results reported in [31] predicted peak adiabatic temperatures within the CNT-PEEK contact zone ranging from 430 to 447 K. This temperature range exceeds the glass transition temperature of PEEK (Tg~416 K [27]). Above Tg, PEEK undergoes a transition to a viscoplastic state, characterized by a sharp drop in yield stress and a significant decrease in the strain-rate sensitivity. Under such conditions, the material response is governed predominantly by the thermal softening component of the Johnson–Cook model (parameter m), whereas the contribution of the strain hardening terms, whose extrapolation represents the primary source of uncertainty—becomes less significant. Although this does not entirely eliminate the extrapolation problem, it substantially reduces its practical impact on the computed stress fields.

The direction of the plastic strain rate tensor $\dot{\boldsymbol{\varepsilon}}^p$ is defined as follows:

$$\dot{\boldsymbol{\varepsilon}}^p = \frac{3}{2}\frac{\mathbf{s}}{\sigma_y}\dot{\bar{\varepsilon}}^p. \quad (10)$$

The evolution of the accumulated plastic strain is expressed via the scalar variable

$$\bar{\varepsilon}^p = \int_0^t \sqrt{\frac{2}{3}\dot{\boldsymbol{\varepsilon}}^p{:}\dot{\boldsymbol{\varepsilon}}^p}dt. \quad (11)$$

In the Johnson–Cook formulation, the total stress tensor is represented as the sum of its deviatoric and hydrostatic components, namely:

$$\boldsymbol{\sigma} = \mathbf{s} - P\mathbf{I}, \quad (12)$$

where $\mathbf{s} = 2G\mathrm{dev}(\boldsymbol{\varepsilon}^e)$ represents the shape distortion (deviatoric stress), and G is the shear modulus; $\mathbf{I}$ is the second-order identity tensor; P is the hydrostatic pressure, which is typically determined using the Mie–Grüneisen equation of state (EOS):

$$P = \frac{\rho_0 c_0^2 \mu \left[1 + \left(1 - \frac{\gamma_0}{2}\right)\mu - a/2\mu^2\right]}{\left[1 - (S-1)\mu\right]^2} + \rho_0 \gamma_0 E, \tag{13}$$

where c_0 is the bulk speed of sound; E is the mass-related internal energy [J/kg]; ρ_0 is the initial material density in its unperturbed (reference) state prior to impact (≈1300 kg/m^3 for PEEK); ρ is the current density of the material at the instant of shock-wave compression; $\mu = \frac{\rho}{\rho_0} - 1$ is the nominal volumetric strain or compression parameter. If $\mu > 0$, the material is in a state of compression; if $\mu < 0$, the material is in a state of tension (expansion); S is the slope coefficient of the linear shock Hugoniot ($U_s - u_p$) relationship), which characterizes the material's structural resistance to compression under increasing impact intensities. A higher S value dictates a more rapid pressure increase for a given level of volumetric compression ($S \approx 1.5$ for PEEK [44]); γ_0 is the Grüneisen gamma (a thermodynamic parameter scaling lattice vibrational thermal energy to hydrostatic pressure), which governs the thermal component of the total pressure. A higher γ_0 value implies that even minor deformation-induced heating induces a sharp increase in internal pressure. For solid bodies, it is conventionally assumed that $\rho\gamma = \rho_0\gamma_0$ (i.e., the Grüneisen parameter decreases inversely with compression). a is the volumetric correction coefficient. This is a small, dimensionless correction factor applied to the Grüneisen parameter to account for its non-linear variation under extreme compression. In most standard problems involving metals and polymers, it is set to a = 0. This implies a classical volume-dependent relationship for γ (strictly linear with respect to density), which has been demonstrated to be physically adequate for the PEEK polymer within the investigated pressure range up to 2.5 GPa [44,45].

This model exhibits inherent limitations at specific strain thresholds; under extreme volumetric compression states μ, the denominator can approach zero, thereby inducing a mathematical singularity. To circumvent this issue, numerical codes must implement a limiter on the μ value to prevent division-by-zero errors. For the PEEK polymer, the restrictive condition $\mu \neq 2$ must be enforced.

To enable the system of governing equations to accurately capture crack initiation and material failure (e.g., during the evaluation of penetration depth or material erosion), it must be augmented with the Johnson–Cook damage model [33,34,38]. This formulation introduces a dimensionless damage parameter, ω, which evolves from 0 (intact material) to 1 (complete failure of the element).

Material failure occurs at the moment when the accumulated equivalent plastic strain, $\bar{\varepsilon}^p$, reaches the critical threshold value for failure strain, $\bar{\varepsilon}_f^p$.

$$\omega = \sum \frac{\Delta \bar{\varepsilon}^p}{\bar{\varepsilon}_f^p}, \tag{14}$$

where ω is the failure indicator. When $\omega \geq 1$, the material stiffness decreases significantly, and the element ceases to resist tensile loading.

The critical fracture strain $\bar{\varepsilon}_f^p$ is not a material constant; instead, it evolves as a function of the stress state, strain rate, and temperature:

$$\bar{\varepsilon}_f^p = \left[d_1 + d_2 e^{(d_3 \eta)}\right]\left[1 + d_4 \ln\left(\frac{\dot{\bar{\varepsilon}}^p}{\dot{\varepsilon}_0}\right)\right]\left[1 + d_5\left(\frac{T - T_r}{T_m - T_r}\right)\right], \tag{15}$$

where $\eta = \frac{P}{\sigma_{eq}}$ is the stress triaxiality factor; σ_{eq} is the equivalent stress (e.g., the von Mises equivalent stress); P is the hydrostatic pressure derived from the Mie–Grüneisen equation of state; $\frac{T - T_r}{T_m - T_r}$ represents the homologous temperature (a dimensionless thermal variable); and d_1–d_5 are material failure parameters determined experimentally from mechanical testing.

For the PEEK polymer, typical values for parameters d_1–d_5 were adopted from [36] and validated for the high-strain-rate regimes characteristic of cold gas dynamic spraying (CGDS): d_1 represents the initial plasticity at zero hydrostatic pressure; d_2 is the exponential coefficient of plasticity growth; d_3 is the sensitivity coefficient to the triaxial stress state; d_4 is the strain rate sensitivity coefficient; and d_5 governs the thermal softening effect).

The material softening effect (the constitutive law of the "degraded" material) is accounted for by modifying the total stress tensor $\boldsymbol{\sigma}$ within the governing equations as:

$$\widetilde{\boldsymbol{\sigma}} = \boldsymbol{\sigma}(1-\omega). \tag{16}$$

Consequently, solving the formulated problem in its fully coupled form requires a system of 16 governing equations—one heat conduction equation, three equations of motion, six constitutive physical equations, and six plastic flow equations—corresponding to 16 unknowns (temperature T as a scalar variable, three displacement components u_i or three velocity components v_i, six components of the stress tensor σ_{ij}, and six components of the plastic strain tensor σ^p_{ij}).

Within the Johnson–Cook framework, all equations are rigorously coupled via the non-linear material parameters A, B, C, n, and m. In this configuration, plastic deformation exhibits a direct dependency on the strain rate logarithm and the local thermal state, rendering the governing system highly coupled (wherein localized temperature changes instantaneously induce material softening).

To solve the contact problem governing the impact of the two-body system (CNT–PEEK), the boundary conditions are partitioned into classical conditions (enforced on the external boundaries Ω_1 and Ω_2) and contact conditions (enforced on the interaction interface Γ_i). The system of governing equations is supplemented by the following boundary conditions:

1. **Classical Boundary Conditions (on External Boundaries).**

   Mechanical Conditions:

- **Dirichlet (Kinematic): $\mathbf{u} = \mathbf{u}^0$** on Γ_u (prescribed displacements or structural constraints); $v = v^0$ on Γ_v (prescribed velocities).
- **Neumann (Static): $\boldsymbol{\sigma}\cdot\mathbf{n} = \mathbf{t}^0$** on Γ_σ (prescribed external tractions or pressure).

   Thermal Conditions:

- **Dirichlet:** $T = T^0$ on Γ_T (prescribed temperature).
- **Neumann:** $-\lambda\nabla T\cdot\mathbf{n} = q_s$ on Γ_q (prescribed surface heat flux q_s).
- **Convective:** $-\lambda\nabla T\cdot\mathbf{n} = h(T - T^{env})$ (convective heat transfer with heat transfer coefficient h to the ambient environment at temperature T^{env}).

2. **Contact Conditions (on the Interface Γ_c):**

   Mechanical Contact:

- **Normal Contact (Karush–Kuhn–Tucker conditions):** The contact pressure is defined as $P_c = \mathbf{n}\cdot\boldsymbol{\sigma}\cdot\mathbf{n} \leq 0$, where $\mathbf{n}$ is the outward unit normal vector to the surface of body Ω_1 directed toward body Ω_2. Non-penetration dictates that the clearance $g \geq 0$, enforcing the complementarity condition $P_c\cdot g = 0$.
- **Friction (Coulomb's Law):** The interfacial shear stress satisfies $|\boldsymbol{\tau}_c| \leq \mu|P_c|$. If $|\boldsymbol{\tau}_c| < \mu|P_c|$, no relative slipping occurs, and the relative velocity vector vanishes: $\mathbf{V}_{rel} = 0$. If $|\boldsymbol{\tau}_c| = \mu|P_c|$, macro-slip initiates, and the frictional shear stress vector opposes the direction of relative velocity: $|\boldsymbol{\tau}_c| = -\mu|P_c|\frac{\mathbf{V}_{rel}}{|\mathbf{V}_{rel}|}$, where μ is the friction coefficient.

Thermal Contact:

Heat exchange and frictional thermal energy generation occur simultaneously at the contact interface separating bodies Ω_1 and Ω_2:

$$-\lambda_1 \nabla T_1 \cdot \mathbf{n}_1 + \lambda_2 \nabla T_2 \cdot \mathbf{n}_2 = q_{fric}$$

- **Contact Thermal Conductance:** The conductive heat flux q_{cont} crossing the interface between the two bodies is defined as $q_{cont} = h_c(T_2 - T_1)$, where h_c is the contact thermal conductance coefficient, which operates as a function of the local contact pressure $\mathbf{P}_c$.
- **Frictional Heat Generation:** The thermal flux generated by micro-slip friction is computed as $q_{fric} = \eta_f(\boldsymbol{\tau}_c \cdot \mathbf{V}_{rel})$, where η_f is the fraction of frictional work converted into thermal energy, which is subsequently partitioned between the two contacting bodies. Due to the extreme disparity in thermal conductivities ($\lambda_{CNT} \gg \lambda_{PEEK}$), the overwhelming majority of the generated frictional heat is instantaneously dissipated through the nanotube structure, which is a critical factor for maintaining the thermal stability of the interface.

Numerical analysis of high-velocity interaction in the "nanotube-polymer substrate" system presents a computational challenge due to the pronounced geometric and physical nonlinearity of the process, driven by high strain rates ($\dot{\varepsilon} > 10^6$ s^{-1}) and intense adiabatic heat generation in the contact zone. To solve the governing equations of the dynamic contact problem within the framework of solid mechanics, traditional Lagrangian and Eulerian formulations are employed, alongside hybrid approaches—namely, the coupled Eulerian–Lagrangian method (CEL) and the arbitrary Lagrangian–Eulerian method (ALE) [30].

In this study, numerical analysis was conducted within the framework of solid mechanics using the finite element method. To investigate the effect of impact angle on carbon nanotube (CNT) embedding, a three-dimensional finite element model (Figure 1) based on the Lagrangian description of continuum motion was adapted and modified [31]. While preserving the geometry of the objects, variability in the direction of the initial velocity vector (V_0) relative to the substrate surface normal was introduced.

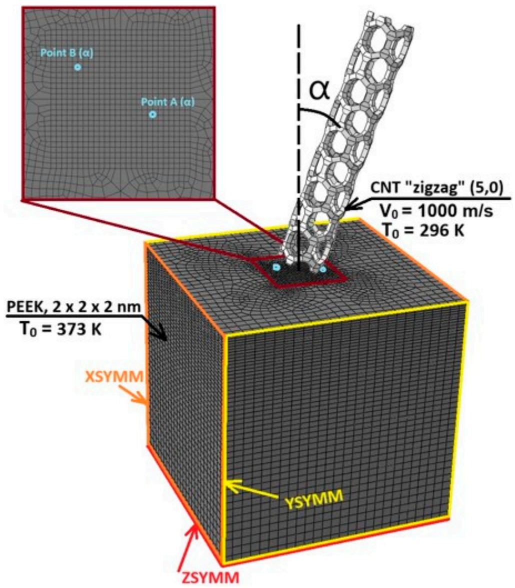

Figure 1. Schematic representation of the three-dimensional finite element model of high-velocity CNT impact at an arbitrary angle α.

This approach enabled detailed tracking of the evolution of the stress–strain state, distribution of equivalent plastic strain fields, and dynamics of temperature gradients arising during oblique impact contact between the CNT and the thermoplastic polymer PEEK.

Calculations were performed using the Abaqus/CAE software package with explicit time integration (Abaqus/Explicit). The selection of this scheme is justified by its high efficiency in modeling short-duration high-energy processes characterized by intense localized deformation and complex contact interactions.

The computational model employs an atomistic-continuum representation of a single-walled carbon nanotube with chirality index (5,0) in a "zigzag" configuration, containing 100 carbon atoms. This aspect ratio was selected to balance physical adequacy and computational efficiency: increasing nanotube length excites transverse bending vibration modes, substantially complicating system dynamics and nonlinearly escalating computational costs, which is impractical for serial parametric analysis.

PEEK was chosen as the substrate material due to its exceptional thermal stability ($T_g \approx 416.15$ K, $T_m \approx 524$ K) and ability to maintain high strength properties under adiabatic heating conditions, making this polymer as a reference material for studying high-velocity loading physics.

To ensure numerical convergence and strict reproducibility of the findings, the three-dimensional computational domain of the PEEK substrate was modeled as a cube with fixed spatial dimensions of $2 \times 2 \times 2$ nm. Discretization was performed using 8-node thermally coupled linear bricks with reduced integration and hourglass control (C3D8RT). Within the active high-velocity contact patch, mesh refinement was implemented down to a minimum cell size of $0.04 \times 0.04 \times 0.04$ nm. This configuration ensured spatial convergence, limiting stress and temperature gradient variations to less than 1.5% compared to a control ultra-fine baseline mesh of 0.02 nm. The total number of unknowns in the computational model was 393,020. The stable explicit time increment was continuously evaluated based on the Courant kinematic stability condition, maintaining a stable time step of $9.8 \cdot 10^{-19}$ s. Artificial mass scaling was strictly omitted to preserve the physical fidelity of inertial forces during high-rate shock wave propagation. The mechanical and thermal contact fields were governed by the General Contact algorithm in Abaqus/Explicit. Tangential behavior was defined via the isotropic Coulomb friction law with a friction coefficient of $\mu = 0.3$. Symmetrical kinematic boundary conditions (XSYMM, YSYMM, ZSYMM) were applied to the bottom and lateral faces of the substrate. It is worth noting that the implementation of symmetry boundary conditions along the peripheral faces of the substrate maintains strict physical validity even under oblique SWCNT impact conditions. The duration of the active impact phase is limited to merely 0.25–0.3 ps. Within this ultra-short transient period, the dilatational and shear acoustic waves propagating through the PEEK matrix at a bulk speed of sound of $c_0 = 2500$ m/s travel a maximum distance of only 0.75 nm. Consequently, the shock wavefront physically cannot reach the peripheral boundaries of the computational domain or reflect back into the active zone during penetration. Thus, the outer boundaries of the model effectively simulate a semi-infinite medium during the interaction window, and the symmetry constraints simply mitigate rigid edge reflections without introducing numerical artifacts into the contact patch. Geometric nonlinearity was incorporated through the NLGEOM option. Initial thermal conditions were set at 373 K for the substrate and 296 K for the CNT within the computational framework.

The mechanical properties of the material (Young's modulus and Poisson's ratio), as well as its specific heat capacity, were defined as temperature-dependent functions, which is crucial for an accurate description of adiabatic shear instability at high strain rates. The room-temperature value of Young's modulus was adopted from. Its temperature dependence was reconstructed based on the relative trends reported in. Specifically, the curve profile from [28] was scaled so that its value at 20 °C matched the reference value from, thereby yielding a consistent temperature-dependent function over the entire investigated temperature range (Figure 2a). The temperature dependence of Poisson's ratio was incorporated using the experimental data reported in [46]. For each isotherm (300, 380, 430, 480, and 520 K), the mean Poisson's ratio was calculated by averaging the scattered data points over the 0–3 GPa pressure range; these mean values were subsequently used as representative simulation inputs. An additional data point at 570 K was introduced based on physical considerations: above the melting temperature, the polymer transitions to a liquid-like state and becomes virtually incompressible, with its Poisson's ratio approaching 0.5 (Figure 2b). The specific heat capacity data were taken from ([29], Figure 5).

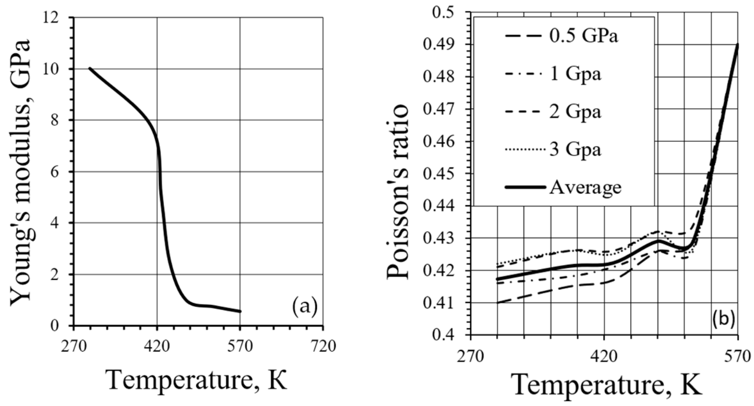

Figure 2. Temperature dependence of PEEK mechanical properties: (**a**) Young's modulus; (**b**) Poisson's ratio.

The mechanical and thermal parameters of the model (Table 1), as well as the Johnson–Cook plasticity model and failure model constants for PEEK (Tables 2 and 3), are comprehensively described in the authors' previous works [31,35].

Table 1. Mechanical and thermal properties for PEEK and CNT.

Properties	Parameters	Unit	Material	
			PEEK	CNT
General	Density, ρ	kg/m^3	1300	1500
	Specific heat capacity, c_v	$J/(kg{\cdot}K)$	$c_v = f(T)$	680
	Thermal conductivity, λ	$W/(m{\cdot}K)$	0.25	3000
	Thermal expansion coefficient, α	$10^{-6}/K$	140	-
	Quinney-Taylor heat fraction coefficient, β	-	0.9	-
Elastic	Young's modulus, E	GPa	$E = f(T)$	6651.4 (bond)
	Poisson's ratio, v	-	$v = f(T)$	0.25

The present study focuses on analyzing the effect of impact angle on the morphology of the plastic flow zone, spatial distribution of contact stresses, and thermodynamic effects arising during the interaction of a high-aspect-ratio nanoparticle with a polymer matrix.

It must be emphasized that deploying a SWCNT model containing 100 carbon atoms represents a deliberate methodological abstraction designed to isolate the elemental contact interaction node at the nanoscale. Under practical cold spray conditions, CNTs are introduced as highly complex, micron-scale agglomerates or long, entangled bundles. However, direct continuum modeling of such extended structures within explicit finite element schemes inevitably excites severe transverse bending modes (the 'whiplash effect'). This numerical artifact triggers catastrophic element distortion and premature simulation termination due to numerical divergence. By investigating an ultra-short SWCNT, the authors decouple the localized interface physics from the macro-scale powder morphology, focusing strictly on the transient thermomechanics of a rigid nano-indenter penetrating a viscoplastic PEEK matrix. This top-down approach successfully defines the fundamental boundary conditions of the nanoscale processing window.

Table 2. Parameters of the Johnson–Cook plasticity model for PEEK [20].

Properties	Parameters	Unit	Value
Johnson–Cook plasticity model	Quasi-steady state yield stress, A	GPa	0.132
	Power law pre-exponential factor, B	GPa	0.0325
	Strain rate pre-exponential factor, C	-	0.1373
	Thermal softening exponent, m	-	2.01
	Strain hardening exponent, n	-	3.5
	Reference strain rate, $\dot{\varepsilon_0}$	s^{-1}	1.0
	Melting temperature, T_m	K	524
	Reference temperature, T_r	K	296

Table 3. Parameters of the Johnson–Cook failure model for PEEK [36].

Properties	Parameters	Value
Johnson–Cook failure model	d_1	0.05
	d_2	1.2
	d_3	−0.254
	d_4	−0.009
	d_5	1

In order to systematically evaluate the effect of the angle of impact on the above parameters, two reference points on the contact interface were chosen: point A and point B (Figure 1), corresponding to the start and end points of contact between CNT and PEEK, respectively.

3. Results

In a previous study by the authors [31], the critical penetration velocity of a single-walled CNT into a PEEK matrix that ensures stable mechanical interlocking was numerically determined to be $\boldsymbol{V_0 = 1000\ \mathrm{m/s}}$. This value was adopted as the baseline parameter for the subsequent analysis of the impact geometry effects. In the present investigation, the impact angle (α) of the initial velocity vector was varied relative to the substrate surface normal. Four specific values were analyzed—0°, 5°, 10°, and 20°—encompassing the technologically permissible range of angular deviations encountered in real-world CGDS processes [22,25]. Special emphasis was placed on the redistribution of the CNT's kinetic energy between its normal and tangential components, as well as its subsequent influence on stress fields, thermal gradients, and the morphology of the penetration zone.

3.1. Dynamics of Stress Fields and Evolution of the CNT Embedding Process and Thermodynamic Effects in the High-Velocity Contact Zone

Figure 3 shows isofields of von Mises equivalent stresses in the PEEK matrix obtained and analyzed at moments t = 0.3, 0.5, and 2.0 ps, spanning the transition from the initial high-velocity contact stage to the residual stress stabilization phase.

Across all computation scenarios, localized adiabatic heating was observed in the contact zone (Figure 4). The peak temperature $\mathbf{T_{max}}$ increases monotonically with impact angle: from 433 K at α = 0° to 447 K at α = 20°. This trend is attributed to the growing contribution of the tangential component: enhanced frictional interaction between the CNT and the viscoplastic PEEK matrix converts a portion of normal deformation energy into heat.

https://doi.org/10.3390/coatings16070843

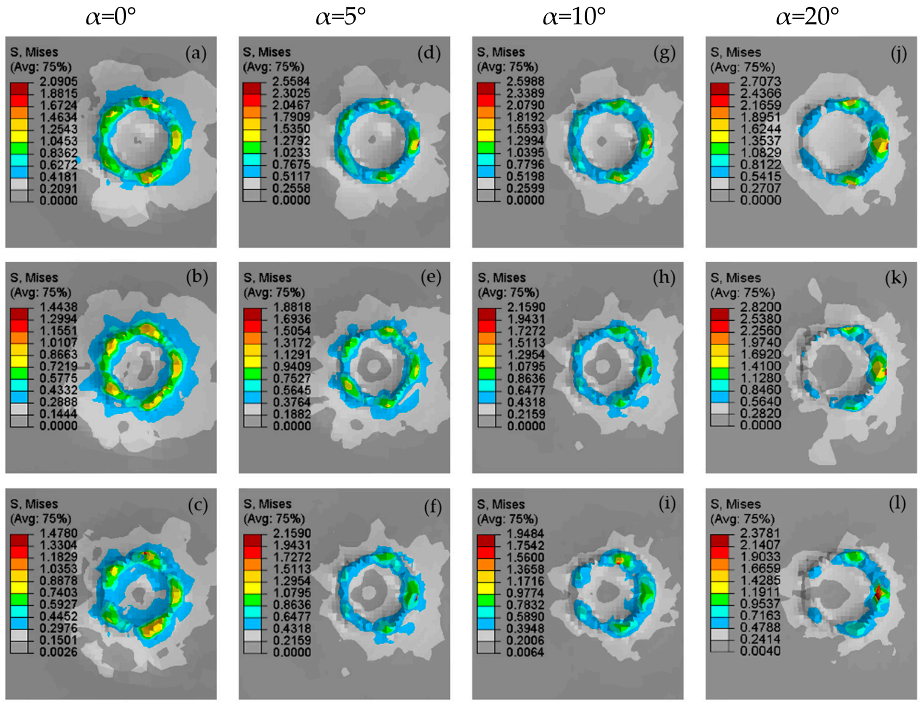

Figure 3. Spatio-temporal evolution of von Mises equivalent stress isofields (GPa) in the PEEK substrate at varying CNT impact angles: (**a**) α = 0°, time = 0.3 ps; (**b**) α = 0°, time = 0.5 ps; (**c**) α = 0°, time = 2 ps; (**d**) α = 5°, time = 0.3 ps; (**e**) α = 5°, time = 0.5 ps; (**f**) α = 5°, time = 2 ps; (**g**) α = 10°, time = 0.3 ps; (**h**) α = 10°, time = 0.5 ps; (**i**) α = 10°, time = 2 ps; (**j**) α = 20°, time = 0.3 ps; (**k**) α = 20°, time = 0.5 ps; (**l**) α = 20°, time = 2 ps.

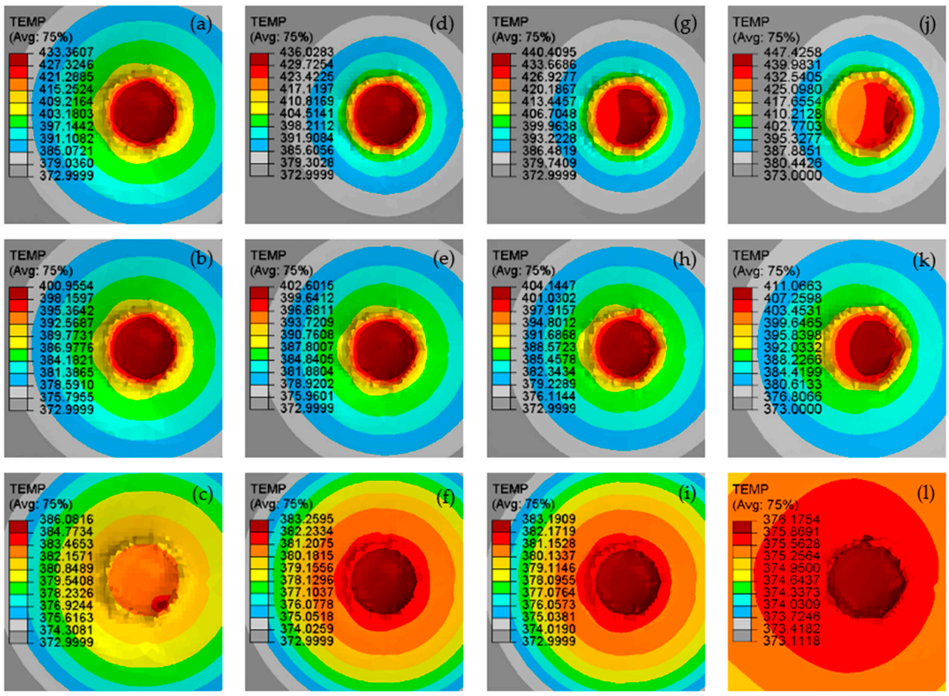

Figure 4. Temperature field distributions (K) in the high-velocity CNT embedding zone in the PEEK substrate at varying impact angles: (**a**) α = 0°, time = 0.3 ps; (**b**) α = 0°, time = 0.5 ps; (**c**) α = 0°, time = 2 ps; (**d**) α = 5°, time = 0.3 ps; (**e**) α = 5°, time = 0.5 ps; (**f**) α = 5°, time = 2 ps; (**g**) α = 10°, time = 0.3 ps; (**h**) α = 10°, time = 0.5 ps; (**i**) α = 10°, time = 2 ps; (**j**) α = 20°, time = 0.3 ps; (**k**) α = 20°, time = 0.5 ps; (**l**) α = 20°, time = 2 ps.

Critically, the recorded T_{max} values exceed the PEEK glass transition temperature ($T_g \approx 416$ K) across all regimes. This, subsequently, indicates that the thermally activated embedding mechanism—localized transition of the matrix to a highly viscoplastic state followed by nanotube fixation upon cooling—is realized at all investigated impact angles. The narrow T_{max} variation ($\Delta T = 14$ K) within the 0–20° range demonstrates the thermal response stability of the system to spray angle variations.

3.2. Kinetics of Plastic Flow and Morphology of the Embedding Zone

The distributions of equivalent plastic strain fields (PEEQ) in the PEEK matrix at various impact angles are shown in Figure 5. At $\alpha = 5°$, the plastic flow zone retains a quasi-axisymmetric character with a uniform annular region of strain hardening surrounding the nanotube. As the impact angle increases, deformations localize on the leading contact side, while their intensity decreases on the trailing side, confirming the growing asymmetry of the stress tensor.

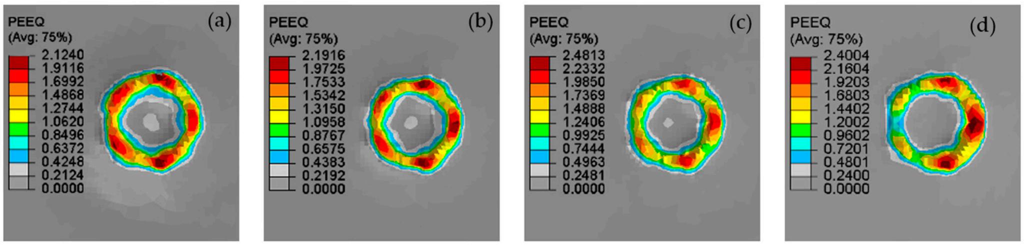

Figure 5. Isofields of equivalent plastic strains in the PEEK substrate during high-velocity CNT embedding at various impact angles: (**a**) $\alpha = 0°$; (**b**) $\alpha = 5°$; (**c**) $\alpha = 10°$; (**d**) $\alpha = 20°$.

The zone of intense plastic flow shifts in the direction of the velocity vector, forming a characteristic material pile-up ahead of the nano-object. All plastic deformation is concentrated within the matrix and described by the Johnson–Cook model. The geometry of the formed crater replicates the profile of the embedded object.

Analysis of PEEQ fields (Figure 5) reveals that at an impact angle of up to 20°, substrate material is not ejected beyond the crater boundaries: deformation exhibits a consolidated character without signs of surface failure. Conversely, the viscoplastic response of PEEK ensures radial constriction of the embedded nanotube by the deformed polymer, as evidenced by the closed configuration of PEEQ isofields surrounding the CNT in Figure 5. This self-wedging effect represents the key factor for mechanical retention of the nanostructure within the thermoplastic matrix.

Representing a single-walled carbon nanotube (SWCNT) within a continuum mechanics framework as a solid elastic body is inherently an idealization. Nevertheless, the deployment of this assumption remains fully valid within the investigated parameter range, as the study strictly focuses on analyzing the PEEK substrate deformation and the stress-field characteristics within the contact zone. For these specific objectives, an elastic continuum representation of the CNT is sufficient and physically accurate (in contrast to its beam-element alternative). Crucially, it must be emphasized that the computational analysis was performed within a fully geometrically non-linear formulation. Furthermore, within the developed continuum framework, treating the nanotube as a solid projectile is physically justified by the spatial and temporal boundary conditions of the problem. Due to the ultra-short length of the (5,0) zigzag SWCNT (~1.2–1.5 nm), its structural axial stiffness is exceptionally high, and its theoretical buckling threshold exceeds the yield resistance of the viscoplastic PEEK matrix by several orders of magnitude. Moreover, during the sub-picosecond impact timeframe (<0.3 ps), higher-order wave-like shell deformation modes do not have sufficient transient time to develop into meaningful amplitudes. Within this specific regime, the SWCNT operates as a quasi-rigid nano-indenter. Interfacial momentum transfer acts as the defining parameter of the process, ensuring that omitting the internal structural deformations of the nanotube introduces no significant numerical artifacts into the calculated macro-stress fields of the substrate.

4. Discussion

Before assessing the discrete molecular response, it is methodologically essential to define the physical validity and inherent limitations of the scale-transition framework used in this study. The direct transfer of macroscopic thermomechanical fields obtained from the continuum-based Finite Element Method (FEM) to the microscopic structure of an individual PEEK monomer represents a phenomenological multi-scale approximation. At the atomic scale, the continuum mechanics is inherently limited by discrete effects, including sub-nanometer stress concentration fluctuations at specific atomic nodes and non-equilibrium ballistic phonon scattering at the CNT–polymer interface. Since the sub-picosecond impact timescale ($t < 0.3$ ps) is comparable to the characteristic relaxation times of acoustic phonons in polymers, local thermal gradients may temporarily deviate from macroscopically averaged temperatures. To bridge this scale gap within physically justifiable boundaries, the continuum parameters (stress tensor components and localized temperature fields) are treated here as a macroscopic thermodynamic energy envelope governing the volume-averaged energy flux into the polymer chain. While this top-down approach neglects atomistic fluctuations, it provides a physically consistent upper-bound boundary condition for statistical partition modeling and identifies the macroscopic driving forces responsible for localized molecular transformations.

Figure 6 presents the time histories of the CNT displacement, localized temperature, von Mises equivalent stresses, and equivalent plastic strains (PEEQ) at characteristic points within the contact zone (A and B, see Figure 1). In all investigated scenarios ($\alpha = 0^\circ, 5^\circ, 10^\circ, 20^\circ$), the displacement curves reach a steady-state plateau within approximately 1.0 ps in the complete absence of elastic recoil, indicating the formation of a stable adhesive bond. The asymptotic convergence of the temperature and PEEQ curves confirms the completion of the thermomechanical relaxation phase within the system.

On the von Mises stress diagram (Figure 6b), all curves exhibit a rapid stress increase immediately upon contact, reaching primary peaks in the range of 0.55–1.0 GPa within the first 0.1 ps. This initial peak corresponds to the first moment of the collision: the normal component of velocity generates a compression wave, which propagates within the PEEK matrix.

Subsequent oscillations in the range $t = 0.1$–0.5 ps result from multiple acoustic wave reflections propagating along the nanotube axis and into the substrate; their damping is governed by adiabatic thermal softening of the matrix (Figure 6c). The anomalous stress peak of approximately 1.43 GPa observed for the contact scenario 10° in Figure 6b at $t \approx 0.3$–0.4 ps arises from a resonant secondary impact: the tangential velocity component excites a bending mode in the nanotube, with accumulated elastic energy released upon reaching maximum embedding depth—a phenomenon referred to here as the whiplash effect. For $t > 1.2$ ps, stresses stabilise at residual values of 0.5–0.9 GPa depending on the impact angle, reflecting a quasi-static residual contact regime; the absence of unloading jumps in the displacement curves confirms the stability of mechanical anchoring across all investigated scenarios.

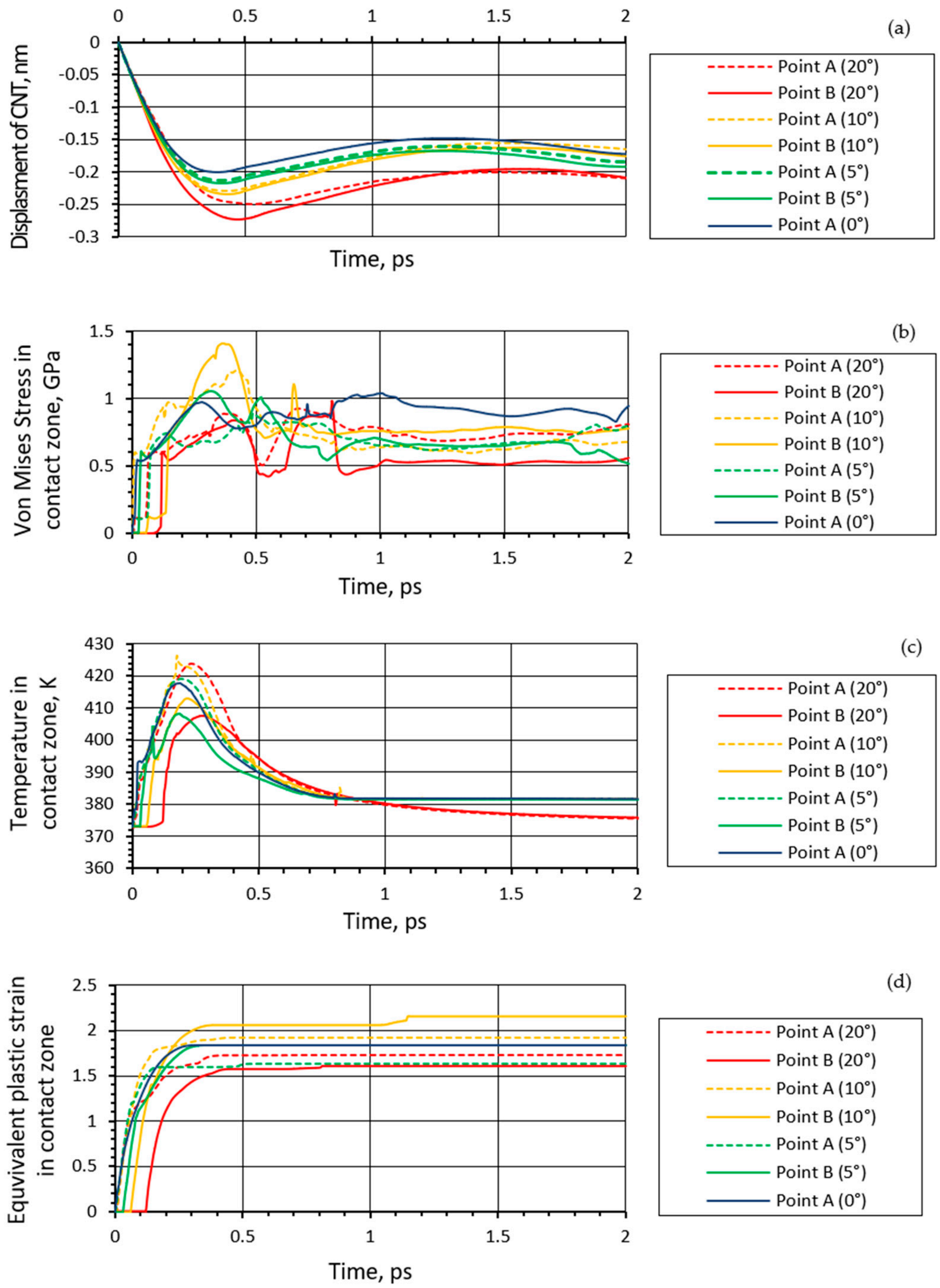

Figure 6. Kinetics of thermomechanical parameters in the CNT−PEEK substrate contact zone at varying impact angles: (**a**) CNT displacement; (**b**) von Mises stresses; (**c**) temperature; (**d**) equivalent plastic strain (PEEQ).

The observed oscillatory stress behaviour is consistent with atomistic modelling results for nano-impact contact [37], where longitudinal acoustic waves propagating through the substrate were reported to produce analogous oscillations in both normal and radial stress components during CGDS of Ti nanoparticles onto Si substrates.

The CNT displacement curves (Figure 6a) demonstrate consistent dynamics across all angles: rapid penetration (t ≈ 0.3–0.5 ps) to the maximum depth, followed by partial elastic relaxation and a plateau by t ≈ 1.0–2.0 ps. The stabilized penetration depth logically increases with the impact angle—from ≈0.18 nm at $\alpha = 0^\circ$ to ≈0.2 nm at $\alpha = 20^\circ$—reflecting the accurate accounting for the reduction in the contact zone area during oblique impact compared to frontal impact.

Critically, complete absence of elastic rebound across all scenarios indicates the irreversible nature of embedding.

Temperature curves (Figure 6c) confirm the adiabatic character of the process: peak heating (430–447 K) is reached within the first 0.1–0.2 ps, followed by monotonic decay due to thermal conduction into the substrate bulk. Across all regimes, peak values exceed T_g PEEK, enabling transient transition of the matrix to a highly elastic state and thermally activated nanotube embedding. The range of peak temperatures (ΔT = 14 K for $\alpha = 0^\circ - 20^\circ$) demonstrates thermal response stability to spray angle variations.

Equivalent plastic strain curves (Figure 6d) grow synchronously with embedding and stabilize at 1.5 to 2.3, depending on angle. Maximum PEEQ values occur at $\alpha = 20^\circ$, driven by intensified shear deformations from the tangential velocity component. The asymptotic nature of PEEQ curves confirms completion of matrix plastic flow and formation of a stable mechanical anchoring zone.

It is critical to analyze the localized resonant spike in the residual stress fields observed at a collision angle of $\alpha = 10^\circ$ in Figure 6. This non-monotonic peak can be attributed to a transient kinematic bifurcation governed by the specific ratio between the normal (V_n) and tangential (V_τ) components of the initial velocity vector. Under quasi-normal impact conditions ($\alpha = 5^\circ$), the energy primarily dominated by symmetric normal compression of the matrix. However, within the critical transition window near $\alpha = 10^\circ$, the magnitude of V_τ becomes sufficient to induce a pronounced asymmetric shear loading, while the still-dominant V_n component resists free interfacial sliding. This This combination of competing normal and tangential loading components causes an instantaneous dynamic pinning of the nano-indenter's leading edge. The resulting transient rotational moment induces high-frequency transverse bending oscillations, generating strongly localized stress concentrations within the PEEK matrix. As the collision angle shifts further to $\alpha = 20^\circ$, the tangential momentum becomes the dominant deformation mechanism, facilitating stable wedge-shaped crater formation through a sliding-dominated contact mode. Consequently, the transient oscillatory response is reduced, leading to the attenuation of the localized stress peak.

The formation of a covalent bond (chemical cross-linking) strictly requires the simultaneous fulfillment of two distinct conditions: a thermal factor (overcoming the activation energy barrier) and a mechanical factor (forcing atoms into close proximity within the range of interatomic forces under applied pressure).

The pronounced localization of equivalent plastic strain (PEEQ) observed at an impact angle of 20° exerts a defining influence on the efficiency of the resulting mechanochemical nano-welding. In classical thermodynamics, a minor temperature increment of ΔT = 14 K (rising from 436 K at 5° to 447 K at 20°) would be insufficient to significantly accelerate chemical reactions. However, under the extreme transient conditions of supersonic impact, the probability of chemical bond formation is governed by a synergetic mechanochemical activation mechanism rather than purely thermal kinetics. The elevated PEEQ at 20° represents an intensive mechanical shear field that forces the severe distortion and elongation of PEEK macromolecular chains along the sliding interface. This severe shear deformation directly prestresses the backbones of the polymer, systematically lowering the activation energy barrier required for the cleavage of the $C_{arom} - O$ ether linkages. Consequently, the mechanical strain primes the molecular structure for dissociation. Within this mechanically destabilized zone, the modest 14 K thermal increment changes its physical role: it no longer serves as the sole initiator of bond rupture, but acts as a highly efficient kinetic catalyst. Because the energy barriers are already compromised by the intense shear field, this additional thermal energy is sufficient to exponentially increase the frequency of successful bond cleavage and subsequent radical formation. Therefore, the mechanical strain is not neutralized by thermal factors; instead, the high PEEQ at a 20° oblique impact establishes a coupled thermo-mechanical state that optimizes the conditions for localized nanoscale encapsulation and chemical bonding.

Analysis of the numerical simulation results for the high-velocity impact of the CNT onto the PEEK substrate at a velocity of V_0 = 1000 m/s reveals a complex thermomechanical nature governing interface formation. The computed peak equivalent von Mises stresses within the PEEK matrix σ_{Mises} = 2.09−2.70 GPa and the maximum localized temperature $T_{max} \approx 447$ K provide a solid foundation to quantitatively evaluate the probability of covalent bond formation between the carbon atoms of the CNT and the atomic framework of the PEEK macromolecules ($C_{19}H_{12}O_3$).

The nanoscale nature of the interaction within the CNT–PEEK system imposes specific boundary conditions on the interfacial energy balance. Due to the negligible mass of a single SWCNT, its kinetic energy at velocities below 600 m/s is insufficient to overcome the potential barrier of the viscoelastic matrix, resulting only in an elastic rebound. A velocity of 1000 m/s provides the requisite momentum for the nano-object to successfully penetrate the near-surface layer of the PEEK [31]. The high peak values of the equivalent stresses and localized temperature are strictly confined to a sub-picosecond temporal window t < 1.0 ps and an ultra-narrow spatial domain. Consequently, this localized thermal flash acts as a kinetic catalyst for mechanochemical nano-welding, driving PEEK into a highly elastic state exclusively within the nanoscale contact patch.

Due to the lack of direct experimental data on the CGDS of single SWCNTs, the reliability of the developed finite element model is justified by strict adherence to the numerical stability criteria. The mathematical reliability of the Abaqus/Explicit numerical scheme is verified by the continuous enforcement of the stable time increment $9.8 \cdot 10^{-19}$ s governed by the Courant kinematic criterion, alongside the complete omission of artificial mass scaling, which prevents any distortion of inertial forces during shock wavefront propagation. Furthermore, the post-peak attenuation behavior of the von Mises equivalent stresses (t > 1.0 ps) and the emergence of localized acoustic oscillations exhibit qualitative agreement with previously reported simulations of nanoscale impact phenomena. The ability of this continuum thermomechanical framework to capture nanosecond-scale wave propagation phenomena and predict the radial encapsulation of the CNT within the viscoplastic PEEK matrix, supports the predictive capability and physical consistency of the proposed methodology reinforces the predictive accuracy and physical validity of the proposed methodology.

Thermomechanical Energy Balance

To quantitatively evaluate the probability of mechanochemical activation, the total energy transferred to a single structural unit of the PEEK macromolecule ($C_{19}H_{12}O_3$) must be first quantified. This repeating structural unit possesses a molecular weight of $M_{CH_{12}O_3} \approx 288$ g/mol [39].

Given a macrostructural PEEK density of ρ = 1300 kg/m^3, the volume occupied by a single structural unit of the PEEK molecule (SUMPEEK), denoted as V_{SUMPEEK}, is computed as:

$$V_{\text{SUMPEEK}} = \frac{M_{C_{19}H_{12}O_3}}{\rho N_A} \approx 3.68 \cdot 10^{-28}\ \text{m}^3 = 0.368\ \text{nm}^3,$$

where $N_A = 6.022 \cdot 10^{23}\ \text{mol}^{-1}$ is Avogadro's number.

Correspondingly, the physical mass of a single SUMPEEK chain segment is given by:

$$m_{\text{SUMPEEK}} = \frac{M_{C_{19}H_{12}O_3}}{N_A} \approx 4.787 \cdot 10^{-25}\ \text{kg}.$$

The total internal energy density transferred to the contact zone is defined as the sum of the mechanical work of plastic deformation and the thermal energy input. Utilizing the quantitative data extracted from the finite element simulations—namely, a peak von Mises stress of σ_{Mises} = 2.7 GPa, (Figure 3j) and an equivalent plastic strain of PEEQ = 2.3, (Figure 6d)—the specific work of plastic deformation per unit volume (strain energy density), denoted as (w), can be evaluated by integrating the product of the stresses and the strain increments:

$$w \approx \int_0^{\bar{\varepsilon}^p} \sigma_{Mises} d\bar{\varepsilon}^p. \quad (17)$$

Under active loading conditions at a constant or averaged stress state, the integration simplifies and can be represented as:

$$w = \sigma_{Mises} \cdot PEEQ = 2.7\,GPa \cdot 2.3 = 6.21 \cdot 10^{-9}\ nJ/nm^3.$$

The mechanical interaction energy transferred per single molecule (SUMPEEK) is subsequently evaluated as:

$$E_{Mech\_unit} = w \cdot V_{SUMPEEK} = 6.21 \cdot 10^{-9}\ nJ/nm^3 \cdot 0.368\ nm^3 = 2.285 \cdot 10^{-9}\ nJ.$$

The energy acquired through localized adiabatic heating from T_0 = 373 K to T_max = 447 K (ΔT = 74 K), given a specific heat capacity of PEEK of c_v = 1340 J/(kg K) [29] (a conservative lower estimate), is determined as:

$$E_{therm\_unit} = c_v \cdot m_{SUMPEEK} \cdot \Delta T = 1340 \cdot 4.787 \cdot 10^{-25} \cdot 74 \approx 4.75 \cdot 10^{-20}\ J = 0.0475 \cdot 10^{-9} nJ.$$

The total internal energy transferred to a single repeating structural unit of the polymer chain is computed as:

$$E_{total\_unit} = E_{Mech\_unit} + E_{therm\_unit} = 2.285 \cdot 10^{-9} + 0.0475 \cdot 10^{-9} = 2.3325 \cdot 10^{-9}\ nJ.$$

A complete topological and quantum-chemical accounting for the repeating structural unit of PEEK, $[-O - C_6H_4 - O - C_6H_4 - CO - C_6H_4-]_n$, establishes exactly N = 37 covalent bonds, partitioned into five distinct functional groups:

1. Intra-ring $C_{arom} - C_{arom}$ bonds within the benzene rings: n_1 = 18 bonds ($D_{e1} \approx 0.83 \cdot 10^{-9}$ nJ).
2. Peripheral $C_{arom} - H$ bonds on the ring boundaries: n_2 = 12 bonds ($D_{e2} \approx 0.7 \cdot 10^{-9}$ nJ).
3. $C_{arom} - O$ linkages (ether bridges): n_3 = 4 bonds ($D_{e3} \approx 0.535 \cdot 10^{-9}$ nJ).
4. $C_{arom} - C_{carb}$ linkages (carbonyl bridges): n_4 = 2 bonds ($D_{e4} \approx 0.575 \cdot 10^{-9}$ nJ).
5. $C = O$ double bonds within the carbonyl group: n_5 = 1 bond ($D_{e5} \approx 1.22 \cdot 10^{-9}$ nJ).
6. Here, D_{ei} is the bond dissociation energy.

Assuming a baseline approximation of uniform energy distribution across the primary skeletal bonds (N = 37 bonds per monomeric unit), the average energy allocated per single bond is defined by: $E_{per\_unit} = \frac{E_{total\_unit}}{N} = \frac{2.3325 \cdot 10^{-9}}{37} \approx 0.06304 \cdot 10^{-9}$ nJ. This uniform allocation corresponds to: $\frac{E_{per\_unit}}{D_{e(C_{arom}-O)}} = \frac{0.06304 \cdot 10^{-9}}{0.535 \cdot 10^{-9}} \cdot 100 = 11.78\%$ of the dissociation energy required for the weakest, most compliant aromatic ether bond $C_{arom} - O$ within the molecular repeat formula of PEEK, $[-O - C_6H_4 - O - C_6H_4 - CO - C_6H_4-]_n$. The fundamental dissociation barrier for this bond is taken as ($D_{e(C_{arom}-O)}$ = 0.535 nN·nm = $0.535 \cdot 10^{-9}$ N$\cdot 10^{-9}$ m = $0.535 \cdot 10^{-18}$ J = $0.535 \cdot 10^{-9}$ nJ) [40].

Achieving an internal energy level of 11.78% of the dissociation threshold under highly dynamic conditions represents a critically important phenomenon.

According to the statistical thermodynamics of deformed polymers [41], under high-velocity shear conditions, localized stress fluctuations at interface non-uniformities (for instance, at the CNT tips, where σ_{CNT} reaches 1.43 GPa) are fully capable of locally exceeding the dissociation barrier D_{e3} [40]. This initiates the homolytic cleavage of the most heavily loaded PEEK bonds, resulting in the generation of free radicals that are prone to direct chemisorption onto structural CNT defects. This process involves the chemical uptake of surrounding macromolecular segments by the solid surface, which predominantly takes place at structural irregularities. These specific defects, such as vacancies, interstitial atoms, and Stone–Wales defects, operate as active sites possessing elevated surface energy, thereby significantly facilitating the formation of robust chemical bonds [42].

Probability of Covalent Cross-Linking

Achieving a total internal energy level of $E_{total\_unit} = 2.3325 \cdot 10^{-9}$ nJ per monomeric unit within a dynamic supersonic impact regime initiates a complex process of intramolecular energy redistribution across the molecular degrees of freedom. From the perspective of statistical thermodynamics and the vibrational spectroscopy of polymers, the assumption of a strictly uniform distribution of the absorbed energy among the macromolecular bonds is physically incorrect [47,48]. The actual vibrational response of the polymer chain is determined by the elastic stiffness (bond force constants, k_{bond}) and the thermodynamic capacity of its constituent linkages.

Under the actual physical conditions of sub-picosecond supersonic impact, the concept of an isoenergetic distribution represents an oversimplification. Due to the pronounced spatiotemporal anisotropy of the stress wavefront and the varying stiffness of PEEK molecular fragments (e.g., rigid aromatic rings versus more labile bridge linkages), the true energy distribution is highly non-uniform. To transition from the idealized baseline assumption to a physically accurate representation of the process, a non-uniform energy distribution model based on the Weibull statistical function is employed. The Weibull statistical approach accounts for the stochastic nature of local microstress concentrations at individual molecular nodes. This approach enables an accurate representation of energy density fluctuations, the overcoming of conformational barriers, and the selective dissociation of the least stable $C_{arom} - O$ ether bonds, thereby establishing a realistic kinetic framework for nanoscale CNT mechanical interlocking.

Therefore, the probability of failure for the entire macromolecular chain, based on the strength distribution of its individual linkages, is evaluated using the weakest-link theory applied to the PEEK molecule under supersonic impact conditions. In contrast to the previously obtained uniform energy allocation of 11.78% per bond, this approach incorporates the statistical nature of bond cleavage under the assumption that the chain ruptures as soon as a single, most heavily loaded or defective bond undergoes dissociation.

The total energy barrier (potential capacity) of all covalent bonds within an isolated monomeric unit is calculated as:

$$\sum_{i=1}^{5} n_i D_{ei} = (18 \cdot 0.83 + 12 \cdot 0.70 + 4 \cdot 0.535 + 2 \cdot 0.575 + 1 \cdot 1.22) \cdot 10^{-9} \approx 27.85 \cdot 10^{-9} \text{ nJ}.$$

Under high-velocity impact loading conditions, the distribution of the absorbed internal energy E_{total_unit} is proportional to the thermodynamic strength and stiffness of the constituent linkages. Within the framework of a quasi-equilibrium approximation during the passage of the shock-wave front, the fraction of energy accumulated by a specific i-th bond is governed by the dimensionless partitioning coefficient $k_{bond} = \frac{D_{ei}}{\sum D_e}$.

For the weakest link of the polymer skeleton—the compliant aromatic ether bond $C_{arom} - O$—this partitioning coefficient is expressed as:

$$k_{C_{arom}-O} = \frac{D_{e_3}}{\sum_{i=1}^{5} n_i D_{e_i}} = \frac{0.535 \cdot 10^{-9}}{27.85 \cdot 10^{-9}} \approx 0.0192 \text{ (or } 1.92\%).$$

Consequently, the actual mechanical and thermal energy transferred to a single $C_{arom} - O$ ether bond at the instant of impact is computed as:

$$E_{C_{arom}-O} = E_{total} k_{C_{arom}-O} = 2.3325 \cdot 10^{-9} \cdot 0.0192 \approx 0.04478 \cdot 10^{-9}\ \text{nJ}.$$

Comparing the acquired energy to the fundamental dissociation barrier of the ether bridge determines its local structural activation level:

$$R = \frac{E_{C_{arom}-O}}{D_{e_3}} = \frac{0.04478 \cdot 10^{-9}}{0.535 \cdot 10^{-9}} \approx 0.0837\ (\text{or } 8.37\%).$$

To evaluate the statistical probability of homolytic bond cleavage, the weakest-link theory is applied based on a three-parameter Weibull distribution function. The failure probability of a single bond, P_{f_bond}, under the current level of energetic interaction is defined by the following expression: $P_{f\_bond} = 1 - e^{-[R]^m}$, where m is the Weibull modulus. For polymer chains, it is conventionally assumed that $m \approx 2 \ldots 4$, reflecting the strength dispersion induced by thermal fluctuations and packing defects.

Assuming a Weibull modulus of (m = 3) for polymer chains subjected to high-velocity shear conditions (reflecting local density fluctuations and spatial distortions of the reaction coordinate geometry according to Zhurkov's kinetic concept [41]), the probability of a single $C_{arom} - O$ bond undergoing cleavage is obtained as:

$$P_{f\_(C_{arom}-O)} = 1 - e^{-(0.0837)^3} \approx 0.00058620.$$

Because the PEEK macromolecule undergoes degradation and subsequent radical generation upon the cleavage of at least a single ether bridge, the integral failure probability of the structural unit, denoted as P_{fail_unit}, is computed via the joint survival probability of all four independent, weak ether linkages:

$$P_{fail\_unit} = 1 - \left(1 - P_{f\_(C_{arom}-O)}\right)^4 \approx 1 - (1 - 0.0005862)^4 \approx 0.0023\ (\text{or } 0.23\%).$$

To transition from the sub-molecular scale of a single CNT to the macroscopic parameters of the deposition spray plume, the volume of the deformation zone (V_{int}) directly beneath the tip of a chiral (5,0) nanotube with a diameter of d = 0.3915 nm must be determined. Assuming that the thickness of the active deformation gradient layer scales with the diameter, $h \approx d = 0.3915$ nm, the interaction volume is computed as:

$$V_{int} = \frac{\pi d^2}{4} h = \frac{\pi \cdot 0.3915^2}{4} 0.3915 = 0.04713 \cdot \text{nm}^3.$$

Consequently, the number of PEEK monomeric units ($V_{unit} \approx 0.368 \cdot \text{nm}^3$) effectively engaged in contact beneath a single nanotube is evaluated as:

$$N_{units} = \frac{V_{int}}{V_{unit}} = \frac{0.04713}{0.368} = 0.128.$$

On the scale of a dense particle ensemble within the deposition spray plume, accounting for the effective spatial packing step of the nanotubes within the matrix (CNT diameter + van der Waals gap = 0.7315 nm), the effective area occupied per single contact footprint is evaluated as $A_{CNT} = 0.535$ nm^2. Consequently, per unit area of the interface (1 μm^2 = 10^6 nm^2), the corresponding density of CNT contacts and engaged polymer structural units are defined as follows:

$$N_{CNT} = \frac{10^6}{0.535} = 1.87 \cdot 10^6 \ \mu m^{-2},$$

$$\sum N_{units} = N_{CNT} \cdot N_{units} = 1.87 \cdot 10^6 \ 0.128 = 2.3936 \cdot 10^5 \ \mu m^{-2}.$$

Given the calculated integral monomer activation probability of 0.23%, the spatial density of chemically activated PEEK segments per 1 μm^2 is expressed as:

$$N_{active} = \sum N_{units} \cdot P_{fail\_unit} = 2.3936 \cdot 10^5 \cdot 0.0023 = 550.5 \ \mu m^{-2}.$$

Considering that each elementary act of homolytic cleavage of the $C_{arom} - O$ bond generates a pair of active free radicals, the total density of radicals at the interface will be equal to:

$$N_{radicals} = 2 \cdot N_{active} = 2 \cdot 550.5 = 1100 \ \mu m^{-2}.$$

The established spatial density of free radicals (~1100 radicals/ μm^{-2}), coupled with the highly elastic state of the polymer matrix ($T > T_g$), is highly sufficient to construct a continuous, three-dimensional network of covalent bridges ("chemical nano-welding") anchored to structural defects on the CNT surface. Concurrently, the absolute structural integrity maintained by 99.77% of the remaining PEEK molecular units strictly demonstrates the complete absence of macroscopic degradation or surface erosion, thereby guaranteeing that the baseline physical–mechanical properties and structural rigidity of the polymer substrate are fully preserved.

"Self-Locking" Mechanism

In addition to chemical bonding, the effect of radial PEEK compression around the embedded nanotube, which was captured during the finite element simulations, plays a vital role in interface stabilization. Following the decay of the primary shock wave, residual stresses within the polymer matrix (reaching up to 0.9 GPa) generate a stable, continuous frictional force field. This confirms that the encapsulation and retention of the CNT within the PEEK substrate during cold gas dynamic spraying possesses a hybrid physical–chemical nature: the dominant mechanical interlocking within the highly elastic polymer domain $T > T_g$ is structurally reinforced by localized covalent cross-linking induced by the local mechanochemical activation.

Contact Duration Analysis

To evaluate the contact duration between the CNT and the PEEK substrate during high-velocity impact, the quantitative time-resolved data extracted from the finite element simulations were analyzed. As demonstrated by the response curves in Figure 3, the active contact duration under peak loading conditions—characterized by a maximum von Mises equivalent stress of 2.7 GPa and a strain energy density of w = $6.2 \cdot 10^{-9}$ nJ/nm^3—is approximately 0.25–0.3 ps. This extremely short interval is sufficient to initiate the elementary events of homolytic bond cleavage. In contrast, the subsequent thermomechanical relaxation phase accompanying CNT penetration extends over more than 2 ns, providing ample time to satisfy the kinetic requirements for the completion of covalent cross-linking ("nano-welding").

The spatial configurations of the embedded CNTs after stabilization (Figure 7) demonstrate that across all investigated impact angles, the nanotube remains securely encapsulated within the near-surface layer of the substrate due to the combined action of residual compressive stresses and impact-induced covalent bonds. Varying the impact angle within the 5–20° range affects the penetration depth and crater asymmetry, but does not compromise the structural integrity of the mechanochemical fixation. It is fundamentally important to distinguish between the timescales governing free radical generation and those regulating subsequent covalent bond recombination at the CNT–PEEK interface. The homolytic scission of the $C_{arom} - O$ ether linkages occurs as a quasi-instantaneous event, triggered by the extreme shear and compressive stress fields within the sub-picosecond impact window (t < 0.3 ps). Conversely, the formation of stable chemical bonds and radical recombination occurs on an extended temporal scale (t > 1.0–2.0 ps) during the thermal and structural relaxation phases of the polymer matrix. The stabilization of the SWCNT within the viscoplastic PEEK trap, alongside the accompanying radial compression (i.e., the pile-up effect), spatially constrains the generated free radicals in close nanoscale proximity to the carbon lattice. This tight spatial confinement effectively bypasses the macroscale radical diffusion stage, drastically accelerating the interaction kinetics between the radicals and SWCNT lattice and ensuring efficient recombination into stable interfacial covalent bonds [49].

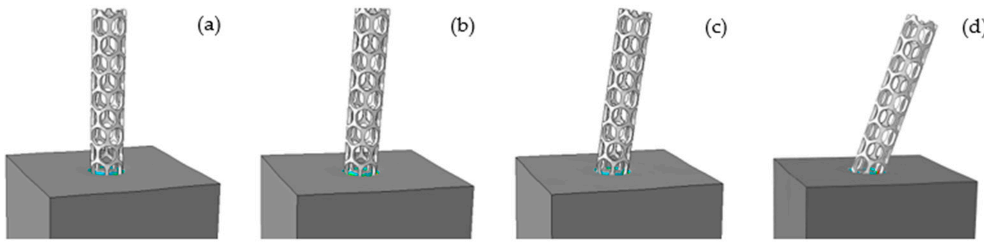

Figure 7. Spatial configuration of the embedded CNT in the PEEK substrate after complete stabilization of thermomechanical parameters: (**a**) $\alpha = 0°$; (**b**) $\alpha = 5°$; (**c**) $\alpha = 10°$; (**d**) $\alpha = 20°$.

The developed finite element framework in Abaqus/Explicit is deployed not as a tool to capture discrete molecular entanglements, but as a phenomenological, space-averaged continuum model. Its primary objective is to evaluate the integrated dissipation balance of kinetic impact energy converted into thermal work. The findings of this study should be interpreted as a mesoscale representation of contact mechanics and mechanochemical activation, rather than an atomistically precise depiction of molecular contact. These volume-averaged thermomechanical metrics subsequently serve as boundary conditions for quantum-statistical estimates of the probability of bond dissociation.

5. Conclusions

Based on a comprehensive finite element analysis combined with a multi-scale thermodynamic evaluation of the high-velocity impact process ($V_0 = 1000$ m/s) of a single-walled chiral (5,0) carbon nanotube (CNT) penetrating a polyetheretherketone (PEEK) substrate at spray angles of 0°, 5°, 10°, and 20°, the following conclusions have been drawn:

1. **Stability of Interface Morphology**: Within the investigated angular range, the oblique impact of the CNT does not induce macroscopic failure of the PEEK matrix surface, as evidenced by the complete absence of material ejection beyond the crater boundaries on the PEQ contour maps. The asymmetric loading conditions generate a distinct "wedge-shaped" penetration zone profile which, in contrast to micrometer-scale metallic systems, significantly increases the actual contact interface area and effectively enhances the mechanical interlocking.
2. **Thermal Activation and Substrate Thermal Softening:** It was established that the peak adiabatic heating within the contact zone (430–447 K) consistently exceeds the glass transition temperature of PEEK across all investigated impact angles. Preheating the substrate to 373 K induces localized thermal softening of the polymer, which in turn triggers a reduction in hydrostatic stiffness. This phenomenon significantly prolongs the duration of the adiabatic compression phase, thereby establishing an

effective "plastic trap" and enabling deep encapsulation of the nanostructure as evidenced by the response histories.

3. **Hybrid Kinetic Retention Mechanism:** The mechanical retention of the CNT is driven by the viscoplastic response of the PEEK matrix, which induces intensive radial compression ("self-locking") around the nanotube via the deformed polymer framework. The rapid transition to a displacement plateau within the 1.0–1.2 ps interval, the complete absence of elastic recoil, and the stabilization of residual quasi-static compressive stresses at a level of 0.5–0.9 GPa (following impact-induced peaks of 2.09–2.70 GPa) collectively substantiate the high mechanical strength of the interface junction.
4. **Selective Mechanochemical Activation:** Based on a comprehensive quantum-chemical topological analysis of the ($C_{19}H_{12}O_3$) monomeric unit, it was demonstrated that the strain energy density at peak stress fields of up to 2.7 GPa generates an internal energy influx of approximately $2.3325 \cdot 10^{-9}$ nJ per molecule. Accounting for the non-uniform energy partitioning proportional to individual bond strengths reveals that the rigid aromatic rings act as structural dampers during impact, whereas the weakest $C_{arom}-O$ ether bond absorbs 1.92% of the total molecular energy, which successfully covers 8.37% of its fundamental dissociation barrier, $D_{e(C_{arom}-O)}$.
5. **Statistical Probability of Chemical Bonding:** The application of the multi-component weakest-link theory based on a three-parameter Weibull distribution enabled the determination that the integral probability of homolytic bond cleavage within a PEEK monomeric unit stands at 0.23%. This quantitative finding confirms the role of specific vulnerable linkages as the dominant chemical initiators of interface interaction, while strictly ruling out the chaotic fragmentation of the rigid benzene rings.
6. **Nanoscale Spatial "Nano-Welding" Effect:** It is demonstrated that at the sub-molecular scale of a chiral (5,0) CNT with a diameter of d = 0.3915 nm, the volume of the deformation zone ($V_{init} = 0.047$ nm^3) is highly localized within a single molecular chain segment. However, upon scaling up to a macroscopic particle ensemble within a dense deposition spray plume, the monomer activation probability of 0.23% guarantees the formation of approximately 1100 active free radicals per square micrometer of the interface. At the nanoscale, this process should not be interpreted as passive degradation; instead, it represents a highly efficient localized mechanochemical activation. The homolytic cleavage of the most labile $C_{arom} - O$ ether linkages within 0.23% of their total population generates an extreme density of unshielded free radicals ($\approx$1100 μm^{-2}) directly inside the nanoscale contact patch. Rather than damaging the material, this controlled chain scission acts as the primary thermodynamic trigger that radically alters the interfacial energy landscape, establishing the necessary kinetic conditions for subsequent nano-welding and stable hybrid encapsulation of the CNT.
7. **Technological and Scientific Significance:** The preservation of penetration efficiency and the structural stability of the mechanochemical bonding across the entire investigated range of spray angles (0–20°) demonstrates the robust reliability of the cold gas dynamic spraying (CGDS) method for the surface modification of PEEK components featuring complex geometries. The kinetics of high-aspect-ratio nanostructures within a viscoplastic matrix under oblique impact conditions were characterized. The findings of this work can be utilized to design functionalized PEEK surfaces with tailored tribological properties.

Author Contributions: Conceptualization, O.H. and S.A.; methodology, O.H. and S.A.; model validation, O.H.; formal analysis, O.H.; investigation, I.Y.; data curation, I.Y.; writing—original draft preparation, O.H.; writing—review and editing, S.A.; supervision, O.H. and S.A. All authors have read and agreed to the published version of the manuscript.

Funding: This research study is funded by the Sponsor–Deutsche Forschungsgemeinschaft (DFG, German Research Foundation)—Project-ID: 554884501 "Multiscale model of deformation and strength characteristics of dispersed carbon nanotube-reinforced polymers".

Institutional Review Board Statement: Not applicable.

Informed Consent Statement: Not applicable.

Data Availability Statement: The original contributions presented in this study are included in the article. Further inquiries can be directed to the corresponding author.

Conflicts of Interest: The authors declare no conflicts of interest.

Abbreviations

The following abbreviations are used in this manuscript:

Acronym	
ABS	Acrylonitrile-butadiene-styrene
ALE	Arbitrary Lagrangian–Eulerian method
CAE	Computer-Aided Engineering
CEL	Coupled Eulerian–Lagrangian method
CGDS	Cold Gas-Dynamic Spraying
CNT	Carbon nanotube
CNT–PEEK	CNT & PEEK composite
$C_{arom} - C_{arom}$	Intra-ring aromatic carbon–carbon bond
$C_{arom} - H$	Aromatic carbon–hydrogen bond
$C_{arom} - O$	Aromatic ether linkage
$C_{arom} - C_{carb}$	Aromatic carbon–carbonyl carbon linkage
$C = O$	Carbonyl double bond
CVD	Chemical vapor deposition
$C_{19}H_{12}O_3$	The chemical formula of the structural unit of the PEEK molecule
ECD	Electrochemical deposition
FEM	Finite Element Method
JC	Johnson–Cook model
LSP	Laser shock peening
MWCNT	Multi-walled carbon nanotube
PEEK	Polyether ether ketone
PEEQ	Equivalent plastic strain (fields)
PEI	Polyetherimide
PVD	Physical vapor deposition
SPH	Smoothed Particle Hydrodynamics
SWCNTs	Single-walled carbon nanotubes
Symbols	
A	Quasi-steady state yield stress (JC), GPa
A_{CNT}	Effective contact footprint area of a single carbon nanotube, nm^2
a	Volume correction factor
B	Power law pre-exponential factor (JC), GPa
C	Strain rate pre-exponential factor (JC)
$\mathbf{C}$	Fourth-rank stiffness tensor, GPa
c_0	Speed of sound, m/s
c_v	Specific heat capacity, J/(kg·K)
$\mathbf{D}$	Total strain rate tensor, s^{-1}
$\mathbf{D}^e$	Elastic strain rate tensor, s^{-1}
$\mathbf{D}^p$	Plastic strain rate tensor
D_e	Bond dissociation energy (Morse potential), nJ
D_{e_1}	Dissociation energy of $C_{arom} - C_{arom}$ bond, nJ

D_{e_2}	Dissociation energy of $C_{arom} - H$ bond, nJ
D_{e_3}	Dissociation energy of $C_{arom} - O$ bond, nJ
D_{e_4}	Dissociation energy of $C_{arom} - C_{carb}$ bond, nJ
D_{e_5}	Dissociation energy of $C = O$ bond, nJ
d	Diameter of CNT, nm
d_1	Initial ductility at zero triaxiality (JC Damage)
d_2	Exponential decay coefficient (JC Damage)
d_3	Triaxiality sensitivity coefficient (JC Damage)
d_4	Strain rate sensitivity coefficient (JC Damage)
d_5	Temperature sensitivity coefficient (JC Damage)
E	Young's modulus, GPa
E_{crit}	Critical dissociation energy threshold, nJ
E_{mech_unit}	Mechanical energy per structural unit, nJ
E_{per_unit}	Energy per skeletal bond, nJ
$E_{\mathrm{therm\_unit}}$	Thermal energy per structural unit, nJ
E_{total_unit}	Total energy per structural unit, nJ
$E_{C_{arom}-O}$	Energy transferred to a sin gle $C_{arom} - O$ bond upon impact, nJ
F	Yield function (yield surface)
$\mathbf{f}$	Body force vector per unit volume, nN/nm^3
G	Shear modulus, GPa
h	Heat transfer coefficient, $W/(m^2 \cdot K)$
h_c	Contact conductance, $W/(m^2 \cdot K)$
I	Second-order identity tensor
k	Thermal conductivity, $W/(m \cdot K)$
$k_{C_{arom}-O}$	Bond energy partition coefficient for $C_{arom} - O$ bond
$M_{C_{19}H_{12}O_3}$	Molar mass of PEEK structural unit
m	Thermal softening exponent (JC)
m_w	Weibull modulus
m_{SUMPEEK}	Mass of PEEK structural unit, kg
N_A	Avogadro's number
N	Total number of covalent bonds per PEEK monomeric unit
N_{units}	Number of PEEK monomeric units
N_{CNT}	Areal density of CNT contact footprints, μm^{-2}
N_{active}	Areal density of mechanically activated PEEK segments, μm^{-2}
$N_{radicals}$	Areal density of generated free radicals at contact interface, μm^{-2}
$\mathbf{n}$	Outward normal vector
n	Strain hardening exponent (JC)
P	Pressure (from Mie-Grüneisen EOS), GPa
P_c	Compressive contact pressure, GPa
P_{f_bond}	Failure probability per skeletal bond
P_{fail_unit}	Failure probability of molecule (weakest link)
$P_{failure}$	Failure probability of structural unit (Weibull)
$P_{f\_(C_{arom}-O)}$	Cleavage probability of a sin gle $C_{arom} - O$ bond
Q	External heat source per unit volume, W/m^3
q_{cont}	Conductive heat flux between bodies, W/m^2
q_{fric}	Frictional heat flux, W/m^2
q_s	Prescribed heat flux, W/m^2
R	Energy activation ratio
S	Slope of shock Hugoniot
$\mathbf{s}$	Deviatoric stress tensor, GPa
T	Current temperature, K
T_0	Initial temperature, K
T^{env}	Environment (ambient) temperature, K
T_g	Glass transition temperature, K

T_m	Melting temperature, K
T_{max}	Peak temperature in contact zone, K
T_r	Reference (initial) temperature (JC), K
T_{room}	Room temperature, K
$\dot{T}$	Temperature rate of change, K/s
t	Time, ps
$\mathbf{u}$	Displacement vector, nm
V_0	Initial velocity, m/s
V_{int}	Interaction volume beneath a single CNT tip, nm^3
$\mathbf{V}_{rel}$	Relative sliding velocity, nm/s
$V_{SUMPEEK}$	Volume of PEEK structural unit, nm^3
V_{unit}	Molar volume of a single PEEK monomeric unit, nm^3
$\mathbf{v}$	Velocity vector, nm/s
υ	Poisson's ratio
$\mathbf{W}$	Spin tensor, s^{-1}
w	Strain energy density, nJ/nm^3
α	Impact angles, °
$\boldsymbol{\alpha}_T$	Thermal expansion tensor, K^{-1}
α_T	Thermal expansion coefficient, K^{-1}
β	Quinney-Taylor heat fraction coefficient
$\dot{\gamma}$	Lagrange multiplier, s^{-1}
γ_0	Grüneisen constant
Γ_c	Contact interface boundary
Γ_q	Thermal boundary (Neumann)
Γ_σ	Static boundary (Neumann)
Γ_T	Thermal boundary (Dirichlet)
Γ_u	Kinematic boundary (Dirichlet)
Γ_v	Velocity boundary
$\boldsymbol{\varepsilon}$	Strain tensor
$\boldsymbol{\varepsilon}^e$	Elastic strain tensor
$\boldsymbol{\varepsilon}^p$	Plastic strain tensor
$\boldsymbol{\varepsilon}^T$	Thermal strain tensor
$\dot{\varepsilon}_0$	Reference strain rate, s^{-1}
$\bar{\varepsilon}_f^p$	Failure (critical) plastic strain
η_f	Friction energy heat fraction
η	Stress triaxiality ratio
$\boldsymbol{\lambda}$	Thermal conductivity tensor W/(m·K)
μ	Compression parameter
ρ	Material density, kg/m^3
ρ_0	Initial material density, kg/m^3
$\boldsymbol{\sigma}$	Stress tensor, GPa
$\dot{\boldsymbol{\sigma}}^\omega$	Jaumann objective stress rate tensor, GPa/s
σ_y	Equivalent yield stress, GPa
σ_{eq};σ_{Mises}	Von Mises equivalent stress, GPa
$\boldsymbol{\tau}_c$	Contact shear stress, GPa
ω	Damage indicator
Ω_i	Solid body domain (i = 1, 2)
(:)	Operator of the double scalar product of tensors
∇	Divergence operators
$-\lambda\nabla T$	Conductive heat flux vector, W/m^2
$\boldsymbol{\sigma}:\dot{\boldsymbol{\varepsilon}}^p$	Plastic dissipation heat source, W/m^3
$\rho c_v \dot{T}$	Rate of change of internal energy, W/m^3
$\mathbf{d}\boldsymbol{\varepsilon}^p$	Incremental plastic strain tensor
$\mathbf{d}\boldsymbol{\gamma}$	Plastic multiplier (incremental)

References

1. Pialago, E.J.T.; Park, C.W. Cold spray deposition characteristics of mechanically alloyed Cu-CNT composite powders. *Appl. Surf. Sci.* **2014**, *308*, 63–74. [CrossRef]
2. Bakshi, S.R.; Singh, V.; Balani, K.; McCartney, D.G.; Seal, S.; Agarwal, A. Carbon nanotube reinforced aluminum composite coating via cold spraying. *Surf. Coat. Technol.* **2008**, *202*, 5162–5169. [CrossRef]
3. Yin, S.; Cavaliere, P.; Aldwell, B.; Jenkins, R.; Liao, H.; Li, W.; Lupoi, R. Cold spray additive manufacturing and repair: Fundamentals and applications. *Addit. Manuf.* **2018**, *21*, 628–650. [CrossRef]
4. Champagne, V.K. (Ed.) Repair of magnesium components by cold spray techniques. In *The Cold Spray Materials Deposition Process: Fundamentals and Applications*; Woodhead Publishing Series in Metals and Surface Engineering; Woodhead Publishing: Sawston, UK, 2007; pp. 327–352. [CrossRef]
5. Lomonaco, P.; Delloro, F. Cold spray on short carbon fiber reinforced PEEK substrates. *Adv. Compos. Hybrid Mater.* **2025**, *8*, 298. [CrossRef]
6. Papyrin, A.; Kosarev, V.; Klinkov, S.; Alkhimov, A.; Fomin, V. *Cold Spray Technology*; Elsevier: Amsterdam, The Netherlands, 2006.
7. Assadi, H.; Gärtner, F.; Stoltenhoff, T.; Kreye, H. Bonding mechanism in cold gas spraying. *Acta Mater.* **2003**, *51*, 4379–4394. [CrossRef]
8. Viesca, F.; de Leon, D.; Alejandro, K.; Ybarra, R.; Rahman, M.W.; Padilla, V.; Vasquez, H.; Lozano, K.; Uddin, M.J. Enhanced triboelectric effect using functionalized multiwalled carbon nanotube-coated fiber mats for biomechanical energy harvesting. *Nano Trends* **2026**, *14*, 100200. [CrossRef]
9. Melentiev, R.; Yu, N.; Lubineau, G. Polymer metallization via cold spray additive manufacturing: A review of process control, coating qualities, and prospective applications. *Addit. Manuf.* **2021**, *48*, 102459. [CrossRef]
10. Karahan, B.; Ozdemir, I.; Grund, T.; Hanisch, N.; Lampke, T. Advancements in cold spraying for polymer matrix composites: Enhanced LSP and EMI shielding performance—Review and future directions. *J. Mater. Sci. Mater. Eng.* **2025**, *20*, 13. [CrossRef]
11. Kalin, M.; Zalaznik, M.; Novak, S. Wear and friction behaviour of poly-ether-ether-ketone (PEEK) filled with graphene, WS 2 and CNT nanoparticles. *Wear* **2015**, *332–333*, 855–862. [CrossRef]
12. Silva, S.; Barbosa, J.M.; Sousa, J.D.; Paiva, M.C.; Teixeira, P.F. High-performance PEEK/MWCNT nanocomposites: Combining enhanced electrical conductivity and nanotube dispersion. *Polymers* **2024**, *16*, 583. [CrossRef] [PubMed]
13. Schmidt, T.; Assadi, H.; Gärtner, F.; Richter, H.; Stoltenhoff, T.; Kreye, H.; Klassen, T. From particle acceleration to impact and bonding in cold spraying. *J. Therm. Spray Technol.* **2009**, *18*, 794–808. [CrossRef]
14. Dykhuizen, R.C.; Smith, M.F. Gas dynamic principles of cold spray. *J. Therm. Spray Technol.* **1998**, *7*, 205–212. [CrossRef]
15. Buhl, S.; Breuninger, P.; Antonyuk, S. Optimization of a laval nozzle for energy-efficient cold spraying of microparticles. *Mater. Manuf. Process.* **2018**, *33*, 115–122. [CrossRef]
16. Parmar, H.; Tucci, F.; Carlone, P.; Sudarshan, T.S. Metallisation of polymers and polymer matrix composites by cold spray: State of the art and research perspectives. *Int. Mater. Rev.* **2022**, *67*, 385–409. [CrossRef]
17. Breuninger, P.; Krull, F.; Huttenlochner, K.; Müller-Reno, C.; Ziegler, C.; Merz, R.; Kopnarski, M.; Antonyuk, S. Microstructuring of steel surfaces via cold spraying with 316L particles for studying the particle-wall collision behavior. *Surf. Coat. Technol.* **2019**, *379*, 125054. [CrossRef]
18. Rokni, M.R.; Feng, P.; Widener, C.A.; Nutt, S.R. Depositing Al-Based Metallic Coatings onto Polymer Substrates by Cold Spray. *J. Therm. Spray Technol.* **2019**, *28*, 1699–1708. [CrossRef]
19. Che, H.; Chu, X.; Vo, P.; Yue, S. Metallization of Various Polymers by Cold Spray. *J. Therm. Spray Technol.* **2017**, *27*, 169–178. [CrossRef]
20. Astaraee, A.H.; Colombo, C.; Bagherifard, S. Insights on metallic particle bonding to thermoplastic polymeric substrates during cold spray. *Sci. Rep.* **2022**, *12*, 18123. [CrossRef] [PubMed]
21. Spitalsky, Z.; Tasi, D.; Papgelis, K.; Galioti, C. Carbon nanotube-polymer composites: Chemistry, processing mechanical and electrical properties. *Prog. Polym. Sci.* **2010**, *35*, 357–401. [CrossRef]
22. Li, W.-Y.; Yin, S.; Wang, X.-F. Numerical investigations of the effect of oblique impact on particle deformation in cold spraying by the SPH method. *Appl. Surf. Sci.* **2010**, *256*, 3725–3734. [CrossRef]
23. Chen, C.; Xie, Y.; Yin, S.; Planche, M.-P.; Deng, S.; Lupoi, R.; Liao, H. Evaluation of the interfacial bonding between particles and substrate in angular cold spray. *Mater. Lett.* **2016**, *173*, 76–79. [CrossRef]
24. Singh, R.; Rauwald, K.H.; Wessel, E.; Mauer, G.; Schruefer, S.; Barth, A.; Wilson, S.; Vassen, R. Effects of substrate roughness and spray-angle on deposition behavior of cold-sprayed Inconel 718. *Surf. Coat. Technol.* **2017**, *319*, 249–259. [CrossRef]
25. Yin, S.; Suo, X.; Su, J.; Guo, Z.; Liao, H.; Wang, X. Effects of substrate hardness and spray angle on the deposition behavior of cold-sprayed Ti particles. *J. Therm. Spray Technol.* **2013**, *23*, 76–83. [CrossRef]
26. Aleksieieva, O.; Bozoglu, M.; Tretiakov, P.; Toporov, A.; Antonyuk, S. Coating of refractory surfaces with fine TiO_2 particles via gas-dynamic cold spraying. *Coatings* **2024**, *14*, 1151. [CrossRef]

https://doi.org/10.3390/coatings16070843

27. Sinnwell, Y.; Maksakov, A.; Palis, S.; Antonyuk, S. Influence of the particle morphology on the spray characteristics in low-pressure cold gas process. *Powder Technol.* **2025**, *464*, 12108. [CrossRef]
28. Maksimov, R.D.; Kubat, J. Time and temperature dependent deformation of poly(ether ether ketone) (PEEK). *Mech. Compos. Mater.* **1997**, *33*, 517–525. [CrossRef]
29. Koerdt, M.; Koerdt, M.; Grobrüg, T.; Skowronek, M.; Herrmann, A.S. Modelling and analysis of the thermal characteristic of thermoplastic composites from hybrid textiles during compression moulding. *J. Thermoplast. Compos. Mater.* **2019**, *35*, 127–146. [CrossRef]
30. Abubakar, A.A.; Al-Athel, K.S.; Ankah, N.; Akhtar, S.S.; Arif, A.F.M. Numerical evaluation of Ni–Al2O3 particles deposition during cold spraying. *J. Mater. Res. Technol.* **2025**, *38*, 226–241. [CrossRef]
31. Gondliakh, O.; Yankovskyi, I.; Antonyuk, S. Features of carbon nanotubes deposition on a polymer substrate by cold gas-dynamic spray technique. *Bull. Natl. Tech. Univ. Ukr.* **2025**, *3*, 9–21. [CrossRef]
32. Tang, W.; Zhang, J.; Li, Y.; Yu, B.; Zhao, J. Numerical Simulation of the Cold Spray Deposition of Copper Particles on Polyether Ether Ketone (PEEK) Substrate. *J. Therm. Spray Technol.* **2021**, *30*, 1792–1809. [CrossRef]
33. Johnson, G.R.; Cook, W.H. Fracture characteristics of three metals subjected to various strains, strain rates, temperatures and pressures. *Eng. Fract. Mech.* **1985**, *21*, 31–48. [CrossRef]
34. Johnson, G.R.; Cook, W.H. A Constitutive Model and Data for Metals Subjected to Large Strains, High Strain Rates and High Temperatures. In Proceedings of the Seventh International Symposium on Ballistics, The Hague, The Netherlands, 19–21 April 1983.
35. Hondliakh, O.; Antonyuk, S.; Weirich, M.; Paas, S. A Coupled Refined Model of Atomistic and Continuum Parameters of Diatomic Covalent Bonds. *Nanomaterials* **2026**, *16*, 347. [CrossRef] [PubMed]
36. Cao, X.; Wu, X.; Meng, X.; Zhang, S.; Song, T.; Ren, P.; Li, T. Numerical Simulation and Experimental Validation of Cutting Mechanism of Carbon Fiber-Reinforced Thermoplastic Composites. *Polymers* **2026**, *18*, 464. [CrossRef] [PubMed]
37. Ghasemi, M.; Seifi, A.; Kateb, M.; Gudmundsson, J.T.; Brault, P.; Marashi, P. Probing trade-off between critical size and velocity in cold-pray: An atomistic simulation. *J. Vac. Sci. Technol. A* **2024**, *42*, 063108. [CrossRef]
38. Sirigiri, V.K.R.; Gudiga, V.Y.; Gattu, U.S.; Suneesh, G.; Buddaraju, K.M. A review on Johnson Cook material model. *Mater. Today Proc.* **2022**, *62*, 3450–3456. [CrossRef]
39. Daoust, D.; Godard, P.; Devaux, J.; Legras, R.; Strazielle, C. Chemical modification of poly(ether ether ketone) for size exclusion chromatography at room temperature: 2. On the reliability of the derivatization procedure for PEEK molecular-mass determination—Application to PEEK-carbon fibre composite. *Polymer* **1994**, *35*, 5498–5503. [CrossRef]
40. Bhuiyan, F.H.; Li, Y.-S.; Kim, S.H.; Martini, A. Shear-activation of mechanochemical reactions through molecular deformation. *Sci. Rep.* **2024**, *14*, 2992. [CrossRef] [PubMed]
41. Zhurkov, S.N. Kinetic concept of the strength of solids. *Int. J. Fract.* **1984**, *26*, 295–307. [CrossRef]
42. Calvi, A.; Ferrari, A.; Sbuelz, L.; Goldoni, A.; Modesti, S. Recognizing Physisorption and Chemisorption in Carbon Nanotubes Gas Sensors by Double Exponential Fitting of the Response. *Sensors* **2016**, *16*, 731. [CrossRef] [PubMed]
43. Zhang, R.; Chen, L.; Xie, K.; Liu, K.; Wu, Z. Compression properties and constitutive model of short glass fiber reinforced poly-ether-ether-ketone (PEEK). *Sci. Rep.* **2023**, *13*, 19206. [CrossRef] [PubMed]
44. Roberts, A.; Appleby-Thomas, G.J.; Hazell, P. Experimental determination of Grüneisen gamma for polyether ether ketone (PEEK) using the shock-reverberation technique. *AIP Conf. Proc.* **2012**, *1426*, 824–827. [CrossRef]
45. Millett, J.C.F.; Bourne, N.K.; Gray, G.T.; Jones, I.P. The response of TiAl based alloys to one-dimensional shock loading. *Acta Mater.* **2002**, *50*, 4801–4811. [CrossRef]
46. Wang, J.; Zhou, Q.; Chao, D.; Li, F.; Cui, T. In situ determination of mechanical properties for poly(ether ether ketone) film under extreme conditions. *RSC Adv.* **2017**, *7*, 8670–8676. [CrossRef]
47. Smalø, H.S.; Rybkin, V.V.; Klopper, W.; Helgaker, T.; Uggerud, E. Mechanochemistry: The Effect of Dynamics. *J. Phys. Chem. A* **2014**, *118*, 7683–7694. [CrossRef] [PubMed]
48. Lloyd, E.M.; Vakil, J.R.; Yao, Y.; Sottos, N.R.; Craig, S.L. Covalent Mechanochemistry and Contemporary Polymer Network Chemistry: A Marriage in the Making. *J. Am. Chem. Soc.* **2023**, *145*, 751–768. [CrossRef] [PubMed]
49. Beyer, M.K.; Clausen-Schaumann, H. Mechanochemistry: The Mechanical Activation of Covalent Bonds. *Chem. Rev.* **2005**, *105*, 2921–2948. [CrossRef] [PubMed]